ACSNANO

www.acsnano.org

ARTICLE

Engineering Thermal Transport across Layered Graphene–MoS_2 Superlattices

Aditya Sood, Charles Sievers, Yong Cheol Shin, Victoria Chen, Shunda Chen, Kirby K. H. Smithe, Sukti Chatterjee, Davide Donadio,* Kenneth E. Goodson, and Eric Pop*

Cite This: *ACS Nano* 2021, 15, 19503–19512

Read Online

ACCESS | Metrics & More | Article Recommendations | Supporting Information

ABSTRACT: **Layering two-dimensional van der Waals materials provides a high degree of control over atomic placement, which could enable tailoring of vibrational spectra and heat flow at the sub-nanometer scale. Here, using spatially resolved ultrafast thermoreflectance and spectroscopy, we uncover the design rules governing cross-plane heat transport in superlattices assembled from monolayers of graphene (G) and MoS_2 (M). Using a combinatorial experimental approach, we probe nine different stacking sequences, G, GG, MG, GGG, GMG, GGMG, GMGG, GMMG, and GMGMG, and identify the effects of vibrational mismatch, interlayer adhesion, and junction asymmetry on thermal transport. Pure G sequences display evidence of quasi-ballistic transport, whereas adding even a single M layer strongly disrupts heat conduction. The experimental data are described well by molecular dynamics simulations, which include thermal expansion, accounting for the effect of finite temperature on the interlayer spacing. The simulations show that an increase of ∼2.4% in the layer separation of GMGMG, relative to its value at 300 K, can lead to a doubling of the thermal resistance. Using these design rules, we experimentally demonstrate a five-layer GMGMG superlattice "thermal metamaterial" with an ultralow effective cross-plane thermal conductivity comparable to that of air.**

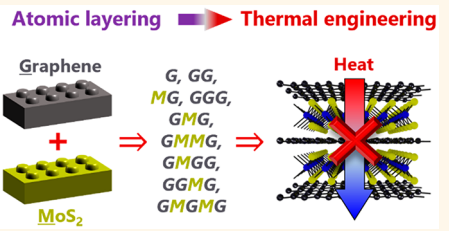

KEYWORDS: *2D materials, van der Waals, heterostructure, phonon, thermal boundary resistance, time-domain thermoreflectance*

Controlling thermal transport at the nanoscale is a major engineering challenge with applications in nanoelectronics, photonics, and energy conversion. Traditional approaches of controlling heat flow have relied on top-down methods, where the thermal conductivity of a material is tuned either through the incorporation of defects[1,2] or *via* a reduction in dimensionality.[3] While these approaches have resulted in the discovery of various regimes of thermal transport, as well as useful applications, they offer limited flexibility in terms of the range of thermal properties that can be accessed. In contrast, two-dimensional (2D) materials offer the ability to engineer thermal transport in a bottom-up manner. Layer-by-layer (LBL) assembly enables the creation of synthetic heterostructures with artificially tailored optical and electronic properties.[4] Because the distribution of atomic masses and bond strengths can be varied on the length scale of individual atoms, it has also been suggested that phonon spectra and thermal transport can be engineered in extreme ways.[5,6] This tunability arises from variations in atomic composition on the scale of phonon wavelengths (few nanometers), as well as large coherence lengths of heat-carrying phonons traveling across van der Waals (vdW) interfaces.[7]

The ability to choose different 2D layers and stack them in a deterministic fashion can enable thermal metamaterials with tailored thermal transport and thermoelectric conversion properties.[8] At the same time, understanding the factors limiting thermal transport at vdW heterointerfaces is crucial for several applications in photonics and nanoelectronics. Energy dissipation creates heat, and interfaces are often the primary bottleneck for cooling a device.[9,10] Using techniques like Raman spectroscopy, time-domain thermoreflectance (TDTR), and time-resolved X-ray diffraction, previous studies have characterized the thermal boundary resistance (TBR) of various vdW interfaces between 2D materials and substrates, as well as between different 2D layers.[11−18] It has generally been found that these interfaces are more thermally resistive than those between isotropic three-dimensional (3D) materials.[18]

Despite these efforts, much remains to be understood about the fundamental mechanisms governing heat transport in vdW superlattices, and a systematic understanding is presently lacking. To design vdW thermal metamaterials, as well as

Received: July 25, 2021
Accepted: November 9, 2021
Published: November 23, 2021

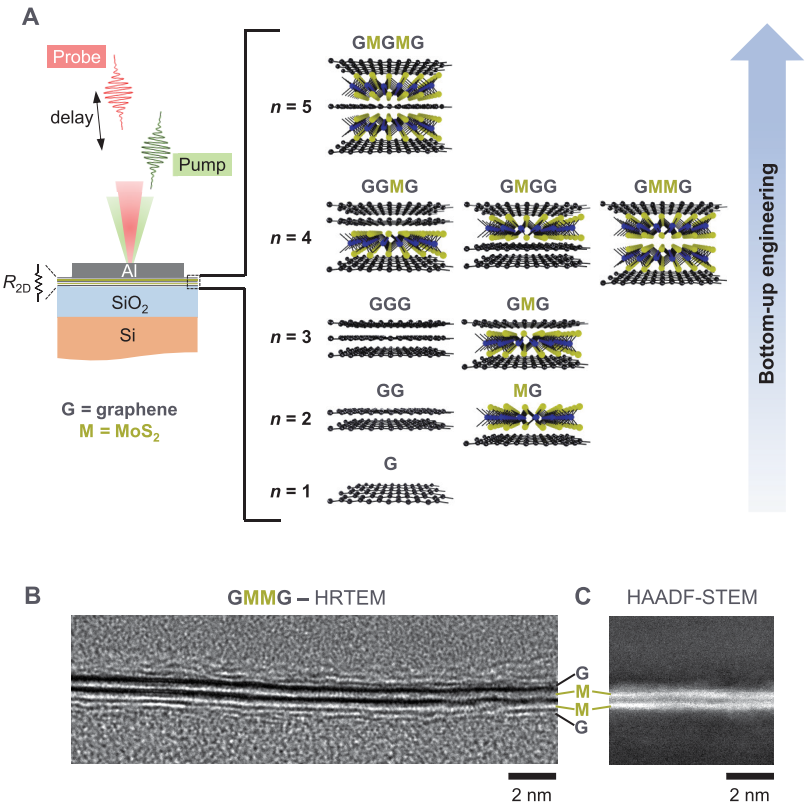

Figure 1. Combinatorial stacking of atomically thin layers. (A) Cross-sectional schematic of the sample, comprising Al (80 nm)/{2D stack}/SiO_2 (90 nm)/Si substrate, where the "2D stack" can be one of nine sequences as shown on the right: G, GG, MG, GGG, GMG, GGMG, GMGG, GMMG, and GMGMG, with *n* denoting the number of layers. (B) High-resolution transmission electron microscope (HRTEM) and (C) high-angle annular dark-field scanning transmission electron microscope (HAADF-STEM) images of a cross section of GMMG.

understand the factors limiting heat dissipation in 2D heterostructure devices, the following questions need to be addressed: What are the primary factors governing thermal transport at vdW junctions; in particular, what are the roles of vibrational mismatch and interlayer separation? How does heat flow across a *hetero*junction compare to that across a *homo*junction? Finally, can we create 3D solids with tailored thermal conductivity by stacking 2D materials with matched or mismatched vibrational modes for a variety of applications?

To shed light on these questions, here, we design an array of LBL-assembled vdW solids made of two dissimilar 2D materials: monolayer graphene (G) and monolayer MoS_2 (M). Through combinatorial stacking of these monolayers, we construct nine sequences, G, GG, MG, GGG, GMG, GGMG, GMGG, GMMG, and GMGMG (see Figure 1), and measure their cross-plane thermal resistance, R_{2D}. This is done using a correlative experimental approach employing TDTR microscopy[2,19] and optical/spectroscopic imaging. Combining experimental results with non-equilibrium molecular dynamics (NEMD), we investigate the effect of layer number (G *vs* GG *vs* GGG and M *vs* MM) and vibrational mismatch (GM *vs* GG and MM) on thermal transport. NEMD simulations with finite-temperature thermal expansion effects accurately predict the thermal resistances of the G, GG, GGG, GMG, and GMMG sequences to within 20% of experimental values. The prediction for the thickest sequence (GMGMG) is ~30% lower than measured. However, it becomes consistent if a larger-than-equilibrium interlayer separation (of only ~1.4%) arising from stacking disorder is considered, as the thermal resistance of the system exhibits a strong dependence on interlayer spacing. Taken together, our results establish design rules governing heat transport in vdW metamaterials. By exploiting these rules, we create a nine-atom-thick "artificial solid" consisting of a graphene/MoS_2 superlattice with an *effective* cross-plane thermal conductivity lower than that of air, making it one of the most effective thermal insulators among fully dense materials.

RESULTS AND DISCUSSION

MoS_2 and graphene monolayers were grown by chemical vapor deposition (CVD) (see Methods for details).[20,21] Heterostructures were assembled by transferring these layers using a polymer-based process onto SiO_2 (90 nm) on Si substrates (see Methods). These substrates were prepatterned with ~50 nm thick Ti/Au alignment markers. Three samples were prepared in all, as follows. Samples D1 and D2 each have up to four layers, containing regions with G, GG, MG, GMG, and GMMG stacking. Both samples were prepared from the same transfer process and were cleaved from a single chip within ~1 cm of each other. Sample D3 contains up to five layers, with regions of GG, GGG, GMG, GGMG, GMGG, and GMGMG stacking. Both D2 and D3 were annealed at 350 °C for 3 h under vacuum (pressure ≈ 7 μTorr) to investigate the effect of interlayer coupling on thermal transport, whereas D1 was not annealed.

Figure 1A shows a schematic of the various stacking sequences grouped by the number of layers *n*. These are (*n* = 1) G; (*n* = 2) GG, MG; (*n* = 3) GGG, GMG; (*n* = 4) GGMG, GMGG, GMMG; and (*n* = 5) GMGMG. A cross-sectional high-resolution transmission electron microscopy

https://doi.org/10.1021/acsnano.1c06299
ACS Nano 2021, 15, 19503−19512

(HRTEM) image of the GMMG stack from the annealed sample D2 is shown in Figure 1B. Four layers are distinguishable, with a total stack thickness of ≈1.7 nm between the top and bottom graphene. Figure 1C shows a high-angle annular dark-field scanning transmission electron microscopy (HAADF-STEM) image, where atomic number contrast enables visualization of the two MoS_2 layers. From this image, we measure the M−M distance to be 0.6−0.7 nm, which is compatible with the 0.616 nm *c*-axis lattice parameter[22] in bulk 2H-MoS_2, indicating good interface quality in our LBL-assembled samples.

To measure the thermal resistance across the stacks, R_{2D}, we used TDTR microscopy (see Methods and Figures S1−S3). The samples were capped with an 80 nm thick Al film using electron-beam (e-beam) evaporation to serve as a transducer (Figure S4). The edges of the prepatterned Ti/Au markers remained visible under an integrated dark-field microscope even after Al deposition, enabling coarse alignment of the sample under the TDTR laser. Finer alignment was achieved by scanning the sample and constructing thermal resistance maps with a pixel size of 0.5 or 1 μm. The full width at half-maximum (fwhm) spatial resolution of this technique is ≈2.2 μm (Figure S5). By comparing the TDTR images with optical micrographs taken before Al capping, a one-to-one mapping was made between the stack configuration and measured R_{2D}. As mentioned before, an important feature of our experiments is the ability to measure multiple stack configurations within the same sample. This is enabled by the finite size (about tens of micrometers) of the triangular MoS_2 monolayers and by tears (missing regions) in the graphene monolayers. Because we probe different regions within a few microns of one another, we can mitigate concerns about spatial variations in the quality of the top (between Al and the top 2D layer) and bottom interfaces (between the bottom 2D layer and SiO_2 substrate) which could otherwise affect the measured R_{2D}. For eight of the nine stacks, the top-most and bottom-most layers are G, which enables direct comparisons of the "intrinsic" stack resistances.

Figure 2A shows an optical image of a region of sample D1. Three stack sequences are distinguishable based on their optical contrast: GG, GMG, and GMMG. MoS_2 photoluminescence (PL) emission measurements made on the same region and are shown in the inset of Figure 2B; the maps plot the intensity integrated over the energy range 1.82 to 1.9 eV. The PL intensity of the MM region is brighter than monolayer M regions, suggesting weak interlayer electronic coupling. As has been shown previously, monolayer MoS_2 is a direct band gap semiconductor with bright PL emission, whereas bilayer MoS_2 (even with an arbitrary twist angle) is indirect band gap with significantly lower PL intensity.[23,24] In the as-prepared sample D1, the MoS_2 layers are weakly coupled, and they behave as individual monolayers whose intensity is approximately doubled in the bilayer region.

Figure 2B displays a TDTR microscopy image of the same region where we plot a colormap of R_{2D}. Details of the mapping technique are provided in the Methods section. A clear correspondence is seen between the optical, PL, and TDTR images. This visual correlation enables a direct extraction of R_{2D} for the different stacking configurations without any image processing. The GMMG region is the most thermally resistive, followed by GMG and GG. The sample also has regions of G and MG stacking, which are not shown in this map. Note that the TDTR measurements were made after

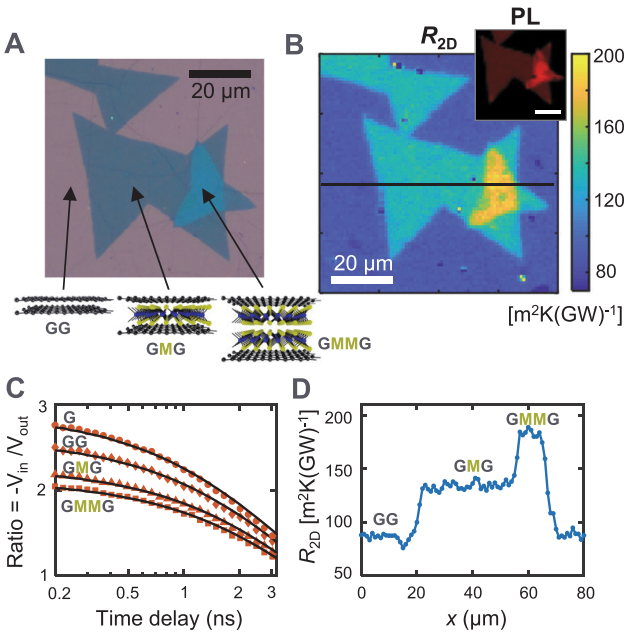

Figure 2. Correlative thermal, optical, and spectroscopic imaging. (A) Optical micrograph of sample D1 with stacks up to GMMG. Three regions are labeled GG, GMG, and GMMG. This sample was not annealed. (B) Map of the thermal resistance between Al and SiO_2 (R_{2D}) measured by TDTR microscopy. Inset: MoS_2 PL map showing brighter signal from GMMG compared to that from GMG due to weak M−M coupling (scale bar 20 μm). A close correspondence is observed between the TDTR, optical, and PL micrographs. (C) TDTR time delay scans showing decay rates decreasing in the order G > GG > GMG > GMMG, corresponding to R_{2D} increasing with layer number. (D) Line scan of R_{2D} along the solid black line in (B).

the sample was coated with an optically opaque 80 nm thick layer of Al; therefore, these results demonstrate the subsurface imaging capability enabled by TDTR microscopy. Single-spot TDTR time scans (over the full range of delays) for each stack configuration are provided in Figure 2C. The decay rate of the ratio ($-V_{in}/V_{out}$) signal encodes information about the interfacial thermal resistance: a faster (slower) rate indicates a lower (higher) R_{2D}. The interfaces show uniformity over large areas, as illustrated by the thermal resistance profile in Figure 2D, which is plotted along the line marked in Figure 2B.

In LBL-assembled vdW stacks, it has been suggested that the interface quality can be improved significantly by high-temperature annealing.[25,26] To probe its effect on interlayer thermal transport, we measure R_{2D} on the annealed sample D2. Figure 3A shows an optical image of a D2 region where five different regions are identified besides bare SiO_2: G, GG, MG, GMG, and GMMG. As discussed above, PL intensity provides a useful means to probe the strength of interlayer electronic coupling. We perform PL mapping of the same sample region (indicated by dash-dotted lines in Figure 3A) before and after the anneal. As demonstrated in Figure 3B, after annealing, there is a crossover in the MoS_2 PL intensity, with GMMG showing quenched emission compared to GMG, consistent with stronger M−M electronic coupling. This is further supported by *in situ* temperature-dependent PL measurements of monolayer and LBL-transferred bilayer MoS_2, as shown in Figures S6 and S7. Note that this quenching is likely not due to enhanced G−M electronic coupling, as the PL intensity of

https://doi.org/10.1021/acsnano.1c06299
ACS Nano 2021, 15, 19503−19512

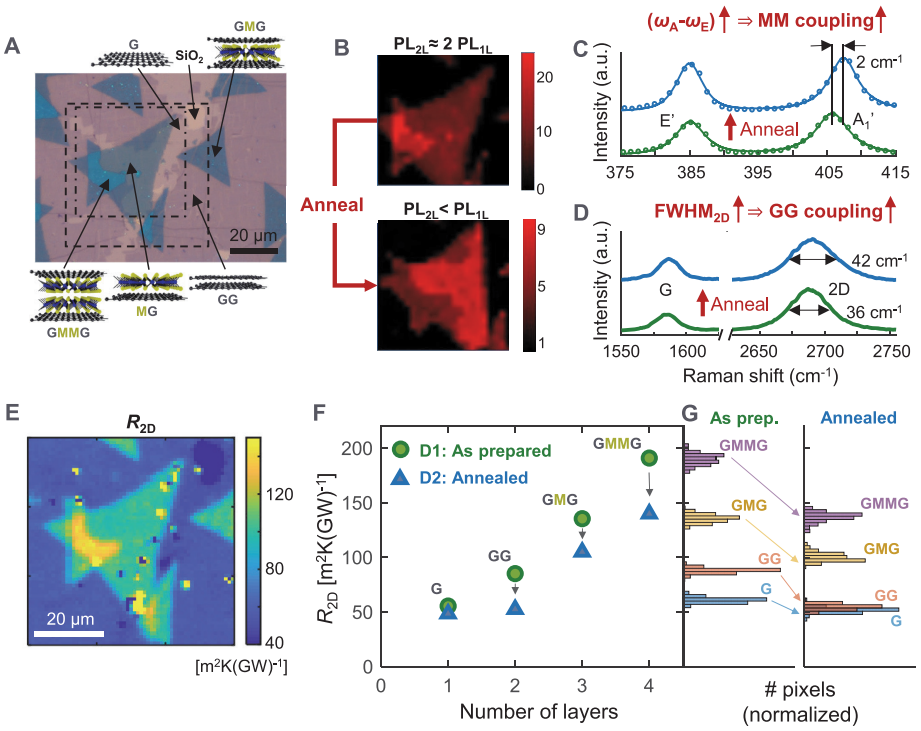

Figure 3. Vacuum annealing tunes interlayer coupling and thermal transport. (A) Optical micrograph of annealed sample D2 showing stacking sequences G, GG, MG, GMG, and GMMG. (B) MoS_2 PL maps of the region marked by the dash-dotted lines in (A) before and after annealing at 350 °C for 3 h under vacuum. A crossover is observed after annealing, with the PL of GMMG becoming quenched relative to GMG, indicating stronger M−M coupling. Note that the sample is rotated by ∼20° in the bottom panel; also, the image is slightly distorted, possibly due to stage drift. (C) MoS_2 Raman spectra of GMMG before (green) and after (blue) annealing. A larger frequency difference between the A_1' and E′ modes suggests enhanced M−M vibrational coupling upon annealing. (D) Graphene Raman spectra of GG before (green) and after (blue) annealing. An increase in the width of the 2D peak and a decrease in the intensity ratio of 2D and G peaks indicates strengthened G−G coupling. (E) TDTR map of thermal resistance (R_{2D}) for the region marked by the dashed lines in (A). (F) R_{2D} of stacks G, GG, GMG, and GMMG in samples D1 (as prepared, *i.e.*, not annealed) and D2 (annealed), extracted from single-spot time scans. Error bars are omitted for clarity (see Table S1 for uncertainty analysis). (G) Histograms of R_{2D} for various stacking sequences based on regions of interest shown in Figures S10 and S11.

GMG does not change significantly on annealing (see Figure S8).

We employ Raman spectroscopy to probe the effect of annealing on interlayer vibrational and electronic coupling. Figure 3C shows that, on annealing, the A_1' peak of MoS_2 in the GMMG region blue shifts, while the E′ peak shows little change. This increased separation by ≈2 cm^{-1} between the A_1' and E′ phonon frequencies indicates stronger M−M vibrational coupling in the annealed sample.[26] This trend is confirmed by *in situ* temperature-dependent Raman measurements on monolayer and LBL-transferred bilayer MoS_2 (Figure S9). Figure 3D plots the Raman spectra of graphene in the GG region before and after annealing. We observe an increase in the fwhm of the 2D peak by ≈6 cm^{-1}. This is consistent with improved G−G electronic coupling and a modification of the electronic band structure in bilayer graphene.[27] The reduced intensity ratio of 2D and G peaks from ∼2.5 to ∼1.8 further supports the notion of enhanced G−G interaction upon annealing.

The sample's thermal resistance map after annealing is shown in Figure 3E, from which we extract R_{GMMG}, R_{GMG}, R_{GG}, and R_G. In Figure 3F, we plot the thermal resistances of the different stack sequences from samples D1 and D2 before and after annealing; these data are extracted by fitting single-spot TDTR time scans over the full delay range. To demonstrate the spatial uniformity of the interfaces, we plot histograms of R_{2D} by defining regions of interest (ROI) in the TDTR maps, as shown in Figure 3G (locations of ROI polygons are given in Figures S10 and S11). We find good agreement between the thermal resistance extracted from the full-delay-time single-spot scans and the fixed-delay-time 2D maps. Spatial variations are relatively small and do not affect our main conclusions. In the unannealed sample D1, we find that R_{2D} scales approximately linearly with the number of layers, such that $R_{GMMG} > R_{GMG} > R_{GG} > R_G$. In comparison, in the annealed sample D2, R_G is similar to D1, but R_{GG} is reduced strongly by ∼40%, such that $R_G \approx R_{GG}$ after the anneal. R_{GMG} and R_{GMMG} also decrease on annealing by ∼23 and ∼27%, respectively. Atomic force microscopy (AFM) measurements show changes in the roughness of GMG and GMMG regions to different degrees, which appear uncorrelated with changes in the thermal resistance (see Figure S12). Taken together with the PL and Raman measurements, these results reveal a strong correlation between the strength of interlayer coupling and thermal resistance of the vdW junctions. Furthermore, the fact that R_{GG} and R_G are similar after annealing, and each is smaller than R_{GMG}, suggests that the intrinsic conductance of a G−G homojunction is significantly larger than that of a G−M heterojunction.

Note that our ability to draw these conclusions is based on our confidence that the Al−G and G−SiO_2 interface resistances do not vary significantly between different regions

https://doi.org/10.1021/acsnano.1c06299
ACS Nano 2021, 15, 19503−19512

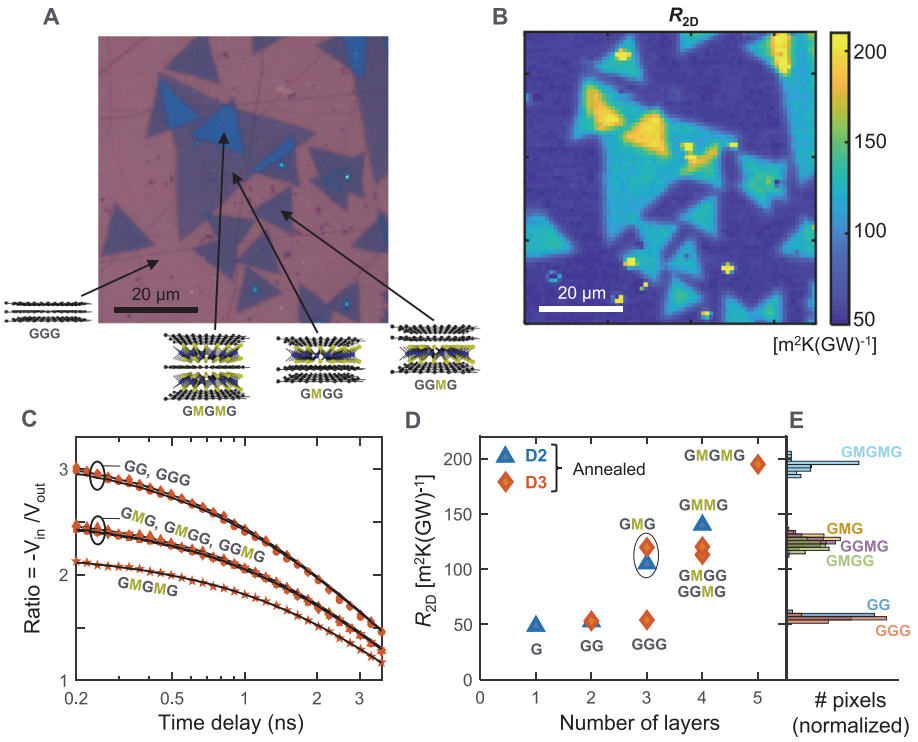

Figure 4. Toward ultralow thermal conductivity in higher-order heterostructures. (A) Optical micrograph of sample D3 showing stacking sequences GGG, GMGG, GGMG, and GMGMG. (B) TDTR map of R_{2D}; note that this sample is annealed. (C) Single-spot TDTR time scans. (D) R_{2D} of all sequences combining data from samples D2 and D3, as extracted from single-spot measurements. Error bars are omitted for clarity (see Table S1). (E) Histograms of R_{2D} for the different stacks in sample D3, based on regions of interest defined in Figure S13. (C–E) Thermal resistances of GGMG and GMGG stacks are nearly identical, implying no thermal rectification. The highest-order GMGMG stack has a thermal resistance that is equivalent to nearly 200 nm of SiO_2 even though it is 100× thinner.

on a sample since they are within ∼100 μm of one another and also do not change substantially upon annealing as R_G is similar before and after the anneal. While we also measure the thermal resistance of MG (≈100 m^2KGW^{-1}), we do not draw any major conclusions from it as its top layer is MoS_2, whose interfacial thermal resistance with Al could be different from that of graphene.

To probe these effects in higher-order stacks, we examine sample D3, which is annealed. Figure 4A,B presents optical microscopy and TDTR thermal resistance maps of a region of the sample that has four stacking sequences: GGG, GMGG, GGMG, and GMGMG. A different region containing GG and GMG sequences is shown in Figure S13. Single-spot delay scans (Figure 4C) show that the temperature decay rates for stacks GG and GGG are very similar, as well as for stacks GMG, GMGG, and GGMG. Consistent with this, an ROI analysis of TDTR maps (Figure 4E) illustrates that the R_{2D} distributions of GG and GGG overlap, as do those of GMG, GMGG, and GGMG. A summary of measurements made on this sample is presented in Figure 4D. The interfacial thermal resistances follow the trend: $R_{GMGMG} > R_{GMGG} \approx R_{GGMG} \approx R_{GMG} > R_{GGG} \approx R_{GG}$.

We make three key observations from the data. First, the strongly coupled (*i.e.*, annealed) G, GG, and GGG interfaces have comparable thermal resistance, indicating that phonon transport across these interfaces is quasi-ballistic. This is shown in D3 by $R_{GGG} \approx R_{GG}$ and in D2 by $R_{GG} \approx R_G$ and is furthermore consistent with the observation that $R_{GMGG} \approx R_{GGMG} \approx R_{GMG}$ (Figure 4C–E). We estimate the *effective* thermal resistance (ρ) of a single G–G junction, ρ_{GG}, using $(R_{GGG} - R_{GG})_{D3}$ and $(R_{GG} - R_G)_{D2}$, which gives $\rho_{GG} < 4$ m^2KGW^{-1}. This is consistent with prior calculations of the cross-plane ballistic thermal resistance of graphite at room temperature,[28] which gave ≈3 m^2KGW^{-1}. Similarly, we also extract the *effective* thermal resistance of an M–M junction, ρ_{MM} using $R_{GMMG} - R_{GMG}$, where R_{GMG} is averaged between D2 and D3; this gives $\rho_{MM} \approx 26$ m^2KGW^{-1}. Our measurements of Al/*n*G/SiO_2 (*n* = 1, 2, 3) are in good agreement with previous data for the thermal resistance of exfoliated few-layer graphene in Au/Ti/*n*G/SiO_2 and Au/Ti/*n*G/Si heterostructures,[17,29] where no strong layer dependence was observed. This similarity between our LBL-assembled CVD-grown layers and prior results on pristine interfaces in exfoliated crystals suggests a good G–G interface quality in our annealed samples. Further, given that our polycrystalline samples are not prepared with a well-defined interlayer twist, this also indicates that turbostratic disorder may not have a strong impact on G–G thermal coupling.

Second, we find that the order of stacking does not affect the total thermal resistance, as $R_{GMGG} \approx R_{GGMG}$. This implies no measurable thermal rectification in such vdW junctions, consistent with prior MD simulations of graphene/MoS_2[30] and other 2D heterojunctions.[31] However, we do not exclude the possibility of rectification under significantly larger thermal gradients, when nonlinearities in the vibrational spectra of G and M lattices may become important.[32] In the present experiments, the vertical temperature gradient is on the order of 1 K nm^{-1}.

Third, the heterojunction G–M is more resistive than the homojunctions G–G and M–M. We estimate the effective G–M resistance using $\rho_{GM} = (R_{GMGMG} - R_G)/4 \approx 37$ m^2KGW^{-1}. Comparing this with the thermal resistances of the

https://doi.org/10.1021/acsnano.1c06299
ACS Nano 2021, 15, 19503–19512

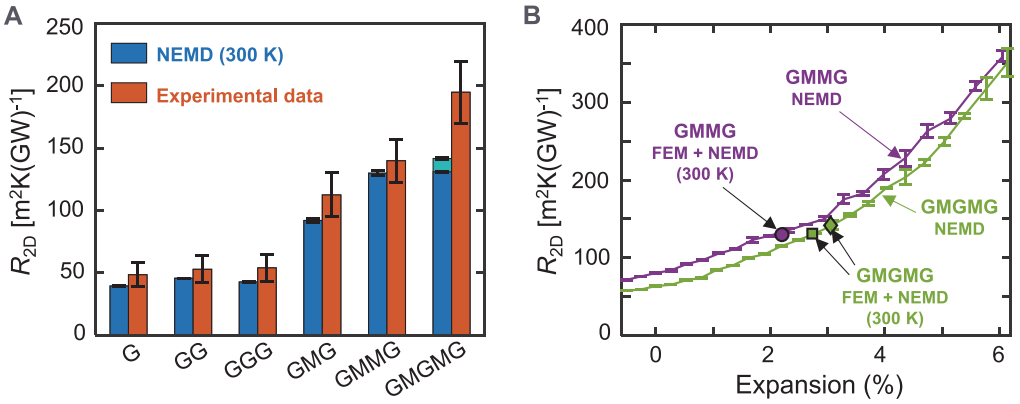

Figure 5. Molecular dynamics simulations and the effect of interlayer spacing on thermal transport. (A) NEMD calculations (blue bars) and experimental data (red bars) for various stacks. NEMD calculations are performed after relaxing each of the structures at 300 K, using a free-energy minimization approach that accounts for finite-temperature effects on the interlayer spacing. For GMGMG, the light blue bar denotes additional resistance when the MM layers are AA *vs* AB stacked. For both theory and experiment, the plotted resistance includes the top and bottom interfaces with the leads. (B) NEMD-calculated thermal resistance of GMMG (purple curve) and GMGMG (green curve) as a function of cross-plane lattice expansion relative to 0 K. Filled markers correspond to stacks with free-energy minimized lattice spacings at 300 K (purple circle, GMMG; green square, GMGMG with AB stacking between M layers; green diamond, GMGMG with AA stacking between M layers).

homojunctions, we summarize the trend as $\rho_{GM} > \rho_{MM} \gg \rho_{GG}$. This trend is consistent with previous MD simulations,[30] which had calculated $\rho_{GM} \approx 3\ \rho_{MM}$ and $\rho_{GM} \approx 15\ \rho_{GG}$. Notably, a single G−M heterojunction consisting of a graphene and MoS_2 monolayer placed only ∼0.5 nm apart has a thermal resistance comparable to ∼50 nm of SiO_2. Equivalently, the GMGMG stack with a thickness of approximately 2 nm (extrapolating from the GMMG TEM in Figure 1B) has an effective cross-plane thermal conductivity (=thickness/resistance) < 0.02 Wm^{-1} K^{-1}. This represents one of the lowest thermal conductivities among dense solids,[12,33] lower than that of dry air at 1 atm and 300 K (∼0.026 Wm^{-1} K^{-1}).[34]

To gain further insights into the mechanisms governing heat transport in vdW stacks, we performed NEMD simulations. The following stacks were simulated to compare with the experiments: G, GG, GGG, GMG, GMMG, and GMGMG. Each stack was enclosed within nine atom thick Al leads. To account for thermal expansion at finite temperature, the structures were relaxed at 300 K using a free-energy minimization (FEM) approach in the quasi-harmonic approximation (QHA).[35−37] As we will show later, thermal expansion is crucial to accurately capture the thermal resistances of the vdW junctions, owing to the strong sensitivity of the TBR to the interlayer spacing. Details of the simulation approach are provided in the Methods (also see Figures S14−S16).

Figure 5A shows the calculated thermal resistances of the various stacks (blue bars) plotted alongside the experimental data (red bars). In the calculations, the plotted results include the resistances of the top and bottom Al−G and G−Al interfaces, whereas in the experiments, they include the Al−G and G−SiO_2 interfaces. In general, good agreement is seen between the trends in the experiments and simulations, with a deviation of <20% for all stacks except GMGMG.

Notably, the simulations show that the resistances of the pure graphene junctions are independent of the number of layers, which is consistent with the measurements. This agreement is noteworthy considering that in the simulations adjacent G layers are AB stacked, whereas in the experiments, the layers are arbitrarily twisted. This suggests that thermal transport across few-layer G−G junctions is quasi-ballistic and may not depend strongly on the interlayer atomic registry. This is also consistent with prior experiments on exfoliated AB-stacked few-layer graphene films where no layer-number dependence was observed in the cross-plane thermal resistance.[17] Next, the simulations predict the trend $R_{GMGMG} > R_{GMMG} > R_{GMG}$, which is consistent with the measurements. For GMGMG, two stacks are simulated, with AB and AA stacking of the M layers; the latter has a resistance that is ∼8% larger than the former. The discrepancy between theory and experiments is the largest for GMGMG at around 30%.

To understand possible reasons behind this, we consider the effect of interlayer spacing on thermal transport. We calculate the cross-plane thermal resistance of GMMG and GMGMG using NEMD, while varying the distance between two fixed layers of Al atoms within the top and bottom leads. In Figure 5B, we plot R_{2D} *versus* the percentage cross-plane lattice expansion relative to its value at T = 0 K (purple and green curves). We see a strong, nonlinear increase in resistance with interlayer spacing. This is qualitatively consistent with prior NEMD simulations[38] and *ab initio* lattice dynamics calculations[39] of the effect of cross-plane tensile strain on the *c*-axis thermal conductivity of pure MoS_2. In Figure 5B, we also plot points corresponding to the expansion and R_{2D} values at 300 K using the FEM approach, which are in good agreement with the 0 K expansion curves. For GMGMG, an increase of ∼2.4% in the layer separation (relative to 300 K) leads to a nearly 100% increase in the thermal resistance. These calculations also suggest that the average interlayer spacing in the GMGMG sample is ∼1.4% larger than the equilibrium spacing at 300 K, which causes NEMD to underpredict the measured resistance by ∼30%. We draw two conclusions from this analysis. First, as the number of layers in the experimental vdW stack increases, the *average* interlayer separation exceeds the equilibrium value, possibly owing to trapped contaminants. Second, the strong sensitivity of the thermal resistance to *c*-axis lattice expansion indicates that extreme care must be taken to ensure cleanliness of heterostructures to be able to make fundamental measurements of interlayer phonon transport.

https://doi.org/10.1021/acsnano.1c06299
ACS Nano 2021, 15, 19503−19512

Finally, to gain insight into the behavior of thicker stacks, we ran NEMD simulations of an 11-layer and a 21-layer stack of alternating G and M layers. For these simulations, we use the equilibrium lattice spacing computed for the GMGMG stack by free energy optimization at 300 K. As expected, the device resistance increases with increasing number of GM layers, but not linearly (Figure S17). This suggests that the transport regime for stacks of less than 21 layers is not yet diffusive, and if the GM stacking is ideal, thicker devices will have lower thermal resistivity. However, while the theoretical onset of diffusive heat transport occurs beyond the thickness of the 21-layer stack, twisting disorder and impurities trapped in the vdW gaps may engender diffusive phonon transport in much thinner stacks. We suggest that the resistivity computed from the 21-layer stack may be used to roughly estimate the resistance of thicker heterostructures.

CONCLUSIONS

In conclusion, using a combinatorial experimental approach we have systematically characterized cross-plane thermal transport in LBL-assembled stacks of monolayer graphene and MoS_2. Using correlative time-domain thermoreflectance and photoluminescence spectroscopy, in conjunction with molecular dynamics simulations, we examined the effects of vibrational mismatch, junction asymmetry, and interlayer coupling strength on heat transport across vdW interfaces. Our results provide a framework for understanding heat flow in vdW metamaterials and enable the creation of artificial solids with ultralow thermal conductivity. More broadly, 2D materials can serve as building blocks for the creation of structures with tailor-made thermal and electronic transport. By layering 2D monolayers with varying degrees of vibrational mismatch and atomic registry (*i.e.*, twist angle and stacking) and leveraging the coupling between lattice and electronic degrees of freedom, there is potentially room for optimizing thermoelectric energy conversion efficiency. Lastly, the insights presented here will also allow for improved engineering of heat flow across vdW heterojunctions in 2D electronics, which is crucial for achieving ultimate performance limits in emerging computing and photonic devices.

METHODS

CVD Growth of Graphene and MoS_2. Continuous monolayer graphene samples were prepared *via* a Cu-mediated low-pressure CVD process. Cu foil (≥99.9% purity, 33 μm thick, JX Nippon Mining & Metals) was placed in a 2 in. quartz tube after being cleaned with acetic acid. After annealing the Cu foil under hydrogen atmosphere at 1040 °C, graphene was synthesized by flowing methane and hydrogen gas at 1040 °C for 40 min. Discontinuous monolayer MoS_2 samples consisting of triangular-shaped crystals were prepared *via* an atmospheric-pressure CVD process on a SiO_2/Si substrate. The SiO_2/Si substrate was first decorated with 20 μL of a perylene-3,4,9,10-tetracarboxylic acid tetrapotassium solution. It was placed in the center of a 2 in. quartz tube facing ∼0.6 mg of MoO_3, while sulfur was located upstream. MoS_2 was synthesized by the interaction between the sulfur carried by 2 sccm of argon inflow and the vaporized MoO_3 on the substrate. To obtain discontinuous monolayers, the growth temperature and time were carefully tailored and adjusted in the range of 700−800 °C and 10−20 min, respectively, and the position of sulfur was optimized. The samples were prepared without controlling the interlayer twist angles.

Polymer-Assisted Transfer Process. Multilayer stacks comprising graphene (G) and MoS_2 (M) monolayers were prepared *via* multiple polymer-assisted layer-by-layer transfer processes. An as-grown graphene film on Cu foil was spin-coated with poly(methyl methacrylate) (PMMA, 950 K A4) and polystyrene (PS, 2.8 g/mol). The Cu foil was etched away by placing the sample in a Cu etchant (CE-100, Transene) for 1 h. The resulting PS/PMMA/G stack was rinsed thoroughly in a deionized water bath. The stack was pinched out of the bath and placed onto an as-grown MoS_2 sample on a SiO_2/Si substrate. Note that the G/M interface did not come in contact with polymer. While maintaining adhesion between graphene and MoS_2, a droplet of water was used to delaminate MoS_2 from the SiO_2/Si substrate,[40] resulting in a PS/PMMA/G/M-stacked sample. Higher-order stacks were prepared by iterating this procedure as required. For example, to assemble the GMGMG stack, the next step involved transferring this stack onto another as-grown graphene sample on Cu foil and repeating the above steps. Note again that the transfer process did not introduce polymer between the 2D layers. The final step involved transferring this stack (*e.g.*, PS/PMMA/G/M/G/M/G) onto a SiO_2 (90 nm) on a Si substrate. The PS/PMMA layers were removed by soaking the sample in toluene.

Time-Domain Thermoreflectance. TDTR is an optical pump−probe technique, which is used to measure thermal conductivity of thin films and TBR of interfaces. Details of this method and our setup are described elsewhere.[2,7,19] Briefly, our setup is based on a 1064 nm, 82 MHz oscillator that produces ∼9 ps pulses. Pump pulses are frequency-doubled to 532 nm by second harmonic generation and amplitude modulated at a frequency of f_{mod} = 10 MHz using an electro-optic modulator. An optically opaque 80 nm thick aluminum transducer layer absorbs the pulses and converts them to heat. As the heat pulses diffuse through the film of interest, in our case, the stack of 2D layers, the temperature decay of the transducer is monitored by measuring the reflected probe intensity as a function of delay time between the pump and probe (0 to 3.7 ns). The measured data consist of the in-phase (V_{in}) and out-of-phase voltage (V_{out}) components of the probe intensity demodulated at f_{mod} using a lock-in amplifier. In a typical measurement, the time series of voltage ratio data ($-V_{in}/V_{out}$) is fit to the solution of a 3D heat diffusion model to extract R_{2D}.

TDTR Mapping. In the present experiments, we adapted the TDTR technique to create maps of R_{2D} by fixing the pump−probe delay time at +250 ps and raster scanning the sample. At each position on the sample, R_{2D} was extracted by comparing the voltage ratio ($-V_{in}/V_{out}$) with a fixed-delay correlation curve obtained from the thermal model (Figure S1). Spatial variations in the interfacial resistance due to different layer stacking appear predominantly as variations in V_{out} (Figure S2). The thickness and thermophysical properties of Al and SiO_2 layers and Si substrate were either measured or taken from literature. In the current experiments, we used a root-mean-square laser spot size of ≈5.1 μm and pump and probe incident powers of approximately 12 and 3 mW, respectively. The estimated steady-state temperature increase is ∼2 K. The fwhm spatial resolution of this technique is ≈2.2 μm (Figure S5). This technique has been used previously to measure spatially inhomogeneous thermal conductivity in polycrystalline diamond,[19] lithium-intercalated MoS_2,[2] and other materials.[14,29,41,42]

Molecular Dynamics Simulations. Interatomic interactions are modeled with empirical potentials tested to reproduce the vibrational properties of graphite, MoS_2, and aluminum. The reparametrized Kolmogorov−Crespi potential was used for interlayer graphene−graphene interactions because of its accuracy in representing the phonon dispersion of graphite along the Γ−A direction (Figure S14).[43] The optimized Tersoff potential was used for intralayer (*i.e.*, in-plane) C−C interactions due to its accurate reproduction of the phonon dispersion of graphene.[44] Graphene−MoS_2 interactions were modeled with a Lennard-Jones potential that was parametrized specifically to study the mechanical properties of graphite−MoS_2 heterostructures.[45] For MoS_2−MoS_2 interactions, we chose the reactive empirical bond-order-type Mo−S potential which has been shown to provide reasonable predictions for the thermal transport properties of MoS_2.[46] The embedded atom model (EAM) was used for Al−Al interactions, which accurately reproduces the phonon dispersion of aluminum (Al).[47] For Al−graphene interactions, we

https://doi.org/10.1021/acsnano.1c06299
ACS Nano 2021, 15, 19503−19512

employed the Morse potential, which was designed for sp^2-carbon modeled by Tersoff and Al modeled by the EAM.[48]

The models were built replicating the commensurate 4:5 MoS_2−graphene hexagonal unit cell, which is made of 4 × 4 MoS_2 unit cells and 5 × 5 graphene unit cells.[49] The resulting GMG cells were then made commensurate with aluminum by creating a 13:3 Al−GMG unit cell using an aluminum face-centered cubic cell with a lattice parameter of 0.286 nm. The (111) Al slabs were placed on both sides of the GMG heterojunctions. We adopt periodic boundary conditions in the plane perpendicular to transport and fixed boundary conditions in the transport direction. The latter were implemented by constraining the coordinates of the outermost layer of Al atoms. We took special care to optimize the interlayer separation in the device by minimizing the free energy with the QHA[35−37] instead of classical MD in the constant pressure canonical ensemble, as the TBR is critically sensitive to cross-plane expansion, as shown by Figure 5B. We minimize the free energy with the QHA because it yields a 0 → 300 K graphite thermal expansion of 1.12%, which is in better agreement with the measured thermal expansion[50] of 1.54% than MD simulations with the Nosé-Hoover barostat, which yields an expansion of 0.53%. The better agreement between QHA thermal expansion and experiment over MD likely results from the inclusion of quantum statistics in the QHA, which help to correctly include the populations of soft flexural modes. The QHA free energy was minimized with respect to *c*-axis expansion and was computed by $F(V,T) = E_{0K}(V) + F_{vib}(V,T)$, where E_{0K} is the total energy of the system at 0 K at a given volume, and F_{vib} represents the vibrational contribution to the free energy:

$$F_{vib} = \sum_{\nu} \frac{\hbar\omega_{\nu}}{2} + \frac{\log(1 - e^{-\beta\hbar\omega_{\nu}})}{\beta}$$

where ω_{ν} are the square roots of the dynamical matrix eigenvalues yielded from all the atoms in the system except for the outer three layers of Al slabs on both sides of the device and $\beta = (k_B T)^{-1}$. The dynamical matrices used for calculating the vibrational free energy were computed with LAMMPS[51] using the finite difference method with an atomic displacement of 10^{-7} nm. Once the interlayer separation was minimized according to the free energy, we calculated the thermal resistance of the devices by NEMD, following the protocol established in ref 52. The outermost layers of Al were fixed while the middle three layers of Al (out of nine layers) on each side were thermostated to 350 and 250 K with a Langevin integrator with a 1 ps relaxation rate. The equations of motion were integrated with a 1 fs time step. NEMD simulations were run, using LAMMPS,[51] for 4.5 ns to ensure that a steady-state heat flux was reached. Simulation configurations and temperature profiles computed in these simulations are shown in Figures S15 and S16.

ASSOCIATED CONTENT

Supporting Information

The Supporting Information is available free of charge at https://pubs.acs.org/doi/10.1021/acsnano.1c06299.

Experimental details: TDTR mapping technique, spatial resolution, sensitivity and error analysis, region-of-interest statistical analysis of thermal resistance maps, *in situ* temperature-dependent PL and Raman measurements, and AFM scans; NEMD simulation details: temperature profiles, simulation cell, and calculations of thicker GM superlattices (PDF)

AUTHOR INFORMATION

Corresponding Authors

Davide Donadio − *Department of Chemistry, University of California, Davis, California 95616, United States;* orcid.org/0000-0002-2150-4182; Email: ddonadio@ucdavis.edu

Eric Pop − *Department of Electrical Engineering, Stanford University, Stanford, California 94305, United States; Department of Materials Science and Engineering, Stanford University, Stanford, California 94305, United States;* orcid.org/0000-0003-0436-8534; Email: epop@stanford.edu

Authors

Aditya Sood − *Department of Electrical Engineering, Stanford University, Stanford, California 94305, United States;* Present Address: Stanford Institute for Materials and Energy Sciences, SLAC National Accelerator Laboratory, Menlo Park, California 94025, United States; orcid.org/0000-0002-4319-666X

Charles Sievers − *Department of Chemistry, University of California, Davis, California 95616, United States*

Yong Cheol Shin − *Department of Electrical Engineering, Stanford University, Stanford, California 94305, United States*

Victoria Chen − *Department of Electrical Engineering, Stanford University, Stanford, California 94305, United States*

Shunda Chen − *Department of Chemistry, University of California, Davis, California 95616, United States*

Kirby K. H. Smithe − *Department of Electrical Engineering, Stanford University, Stanford, California 94305, United States*

Sukti Chatterjee − *Applied Materials Inc., Santa Clara, California 95054, United States*

Kenneth E. Goodson − *Department of Mechanical Engineering and Department of Materials Science and Engineering, Stanford University, Stanford, California 94305, United States*

Complete contact information is available at: https://pubs.acs.org/10.1021/acsnano.1c06299

Author Contributions

A.S., Y.C.S., and E.P. conceived the experiments; A.S. performed the TDTR measurements and analyzed the data; Y.C.S. fabricated the samples with assistance from V.C. and K.K.H.S.; Y.C.S. performed PL and Raman characterization with input from V.C.; C.S. performed the molecular dynamics simulations with input from S.Che. and D.D.; S.Cha. assisted with TEM characterization; A.S. wrote the manuscript with input from C.S., Y.C.S., D.D., and E.P.; D.D., K.E.G., and E.P. supervised the project. C.S. and Y.C.S. contributed equally.

Notes

The authors declare no competing financial interest.

ACKNOWLEDGMENTS

Part of this work was performed at the Stanford Nano Shared Facilities (SNSF) and the Stanford Nanofabrication Facility (SNF), supported by the National Science Foundation (NSF) under award ECCS-2026822. This research was supported in part by the NSF Engineering Research Center for Power Optimization of Electro Thermal Systems (POETS) with cooperative agreement EEC-1449548, by AFOSR Grant No. FA9550-14-1-0251, by NSF EFRI 2-DARE Grant No. 1542883, and by the Stanford SystemX Alliance. We also acknowledge Brookhaven National Lab for allocating computational resources. This research used resources of the Center for Functional Nanomaterials, which is a U.S. DOE Office of

Science Facility, at Brookhaven National Laboratory under Contract No. DE-SC0012704.

REFERENCES

(1) Cho, J.; Losego, M. D.; Zhang, H. G.; Kim, H.; Zuo, J.; Petrov, I.; Cahill, D. G.; Braun, P. V. Electrochemically Tunable Thermal Conductivity of Lithium Cobalt Oxide. *Nat. Commun.* **2014**, *5*, 4035.

(2) Sood, A.; Xiong, F.; Chen, S.; Wang, H.; Selli, D.; Zhang, J.; McClellan, C. J.; Sun, J.; Donadio, D.; Cui, Y.; Pop, E.; Goodson, K. E. An Electrochemical Thermal Transistor. *Nat. Commun.* **2018**, *9*, 4510.

(3) Li, D.; Wu, Y.; Kim, P.; Shi, L.; Yang, P.; Majumdar, A. Thermal Conductivity of Individual Silicon Nanowires. *Appl. Phys. Lett.* **2003**, *83* (14), 2934−2936.

(4) Geim, A. K.; Grigorieva, I. V. van der Waals Heterostructures. *Nature* **2013**, *499*, 419−425.

(5) Guo, R.; Jho, Y. D.; Minnich, A. J. Coherent Control of Thermal Phonon Transport in van der Waals Superlattices. *Nanoscale* **2018**, *10*, 14432−14440.

(6) Hu, S.; Ju, S.; Shao, C.; Guo, J.; Xu, B.; Ohnishi, M.; Shiomi, J. Ultimate Impedance of Coherent Heat Conduction in van der Waals Graphene-MoS_2 Heterostructures. *Mater. Today Phys.* **2021**, *16*, 100324.

(7) Sood, A.; Xiong, F.; Chen, S.; Cheaito, R.; Lian, F.; Asheghi, M.; Cui, Y.; Donadio, D.; Goodson, K. E.; Pop, E. Quasi-Ballistic Thermal Transport across MoS_2 Thin Films. *Nano Lett.* **2019**, *19* (4), 2434−2442.

(8) Sadeghi, H.; Sangtarash, S.; Lambert, C. J. Cross-Plane Enhanced Thermoelectricity and Phonon Suppression in Graphene/MoS_2 van Der Waals Heterostructures. *2D Mater.* **2017**, *4*, No. 015012.

(9) Suryavanshi, S. V.; Gabourie, A. J.; Barati Farimani, A.; Pop, E. Thermal Boundary Conductance of Two-Dimensional MoS_2 Interfaces. *J. Appl. Phys.* **2019**, *126* (5), No. 055107.

(10) Zhao, Y.; Cai, Y.; Zhang, L.; Li, B.; Zhang, G.; Thong, J. T. L. Thermal Transport in 2D Semiconductors — Considerations for Device Applications. *Adv. Funct. Mater.* **2020**, *30*, 1903929.

(11) Yalon, E.; McClellan, C. J.; Smithe, K. K. H.; Munoz Rojo, M.; Xu, R. L.; Suryavanshi, S. V.; Gabourie, A. J.; Neumann, C. M.; Xiong, F.; Farimani, A. B.; Pop, E. Energy Dissipation in Monolayer MoS_2 Electronics. *Nano Lett.* **2017**, *17* (6), 3429−3433.

(12) Vaziri, S.; Yalon, E.; Munoz Rojo, M.; Suryavanshi, S. V.; Zhang, H.; McClellan, C. J.; Bailey, C. S.; Smithe, K. K. H.; Gabourie, A. J.; Chen, V.; Deshmukh, S.; Bendersky, L.; Davydov, A. V.; Pop, E. Ultrahigh Thermal Isolation across Heterogeneously Layered Two-Dimensional Materials. *Sci. Adv.* **2019**, *5*, No. eaax1325.

(13) Liu, Y.; Ong, Z.; Wu, J.; Zhao, Y.; Watanabe, K.; Taniguchi, T.; Chi, D.; Zhang, G.; Thong, J. T. L.; Qiu, C.-W.; Hippalgaonkar, K. Thermal Conductance of the 2D MoS_2/h-BN and Graphene/h-BN Interfaces. *Sci. Rep.* **2017**, *7*, 43886.

(14) Brown, D. B.; Shen, W.; Li, X.; Xiao, K.; Geohegan, D. B.; Kumar, S. Spatial Mapping of Thermal Boundary Conductance at Metal-Molybdenum Diselenide Interfaces. *ACS Appl. Mater. Interfaces* **2019**, *11* (15), 14418−14426.

(15) Yasaei, P.; Foss, C. J.; Karis, K.; Behranginia, A.; El-Ghandour, A. I.; Fathizadeh, A.; Olivares, J.; Majee, A. K.; Foster, C. D.; Khalili-Araghi, F.; Aksamija, Z.; Salehi-Khojin, A. Interfacial Thermal Transport in Monolayer MoS_2- and Graphene-Based Devices. *Adv. Mater. Interfaces* **2017**, *4*, 1700334.

(16) Hopkins, P. E.; Baraket, M.; Barnat, E. V.; Beechem, T. E.; Kearney, S. P.; Duda, J. C.; Robinson, J. T.; Walton, S. G. Manipulating Thermal Conductance at Metal-Graphene Contacts *via* Chemical Functionalization. *Nano Lett.* **2012**, *12* (2), 590−595.

(17) Koh, Y. K.; Bae, M. H.; Cahill, D. G.; Pop, E. Heat Conduction across Monolayer and Few-Layer Graphenes. *Nano Lett.* **2010**, *10* (11), 4363−4368.

(18) Nyby, C.; Sood, A.; Zalden, P.; Gabourie, A. J.; Muscher, P.; Rhodes, D.; Mannebach, E.; Corbett, J.; Mehta, A.; Pop, E.; Heinz, T. F.; Lindenberg, A. M. Visualizing Energy Transfer at Buried Interfaces in Layered Materials Using Picosecond X-Rays. *Adv. Funct. Mater.* **2020**, *30*, 2002282.

(19) Sood, A.; Cheaito, R.; Bai, T.; Kwon, H.; Wang, Y.; Li, C.; Yates, L.; Bougher, T.; Graham, S.; Asheghi, M.; Goorsky, M.; Goodson, K. E. Direct Visualization of Thermal Conductivity Suppression Due to Enhanced Phonon Scattering near Individual Grain Boundaries. *Nano Lett.* **2018**, *18* (6), 3466−3472.

(20) Smithe, K. K. H.; English, C. D.; Suryavanshi, S. V.; Pop, E. Intrinsic Electrical Transport and Performance Projections of Synthetic Monolayer MoS_2 Devices. *2D Mater.* **2017**, *4*, No. 011009.

(21) Wang, N. C.; Carrion, E. A.; Tung, M. C.; Pop, E. Reducing Graphene Device Variability with Yttrium Sacrificial Layers. *Appl. Phys. Lett.* **2017**, *110*, 223106.

(22) Zhu, G.; Liu, J.; Zheng, Q.; Zhang, R.; Li, D.; Banerjee, D.; Cahill, D. G. Tuning Thermal Conductivity in Molybdenum Disulfide by Electrochemical Intercalation. *Nat. Commun.* **2016**, *7*, 13211.

(23) Mak, K. F.; Lee, C.; Hone, J.; Shan, J.; Heinz, T. F. Atomically Thin MoS_2: A New Direct-Gap Semiconductor. *Phys. Rev. Lett.* **2010**, *105*, 136805.

(24) Liu, K.; Zhang, L.; Cao, T.; Jin, C.; Qiu, D.; Zhou, Q.; Zettl, A.; Yang, P.; Louie, S. G.; Wang, F. Evolution of Interlayer Coupling in Twisted Molybdenum Disulfide Bilayers. *Nat. Commun.* **2014**, *5*, 4966.

(25) Hemmat, Z.; Yasaei, P.; Schultz, J. F.; Hong, L.; Majidi, L.; Behranginia, A.; Verger, L.; Jiang, N.; Barsoum, M. W.; Klie, R. F.; Salehi-Khojin, A. Tuning Thermal Transport through Atomically Thin $Ti_3C_2T_z$ MXene by Current Annealing in Vacuum. *Adv. Funct. Mater.* **2019**, *29*, 1805693.

(26) Jin, K.; Liu, D.; Tian, Y. Enhancing the Interlayer Adhesive Force in Twisted Multilayer MoS_2 by Thermal Annealing Treatment. *Nanotechnology* **2015**, *26* (40), 405708.

(27) Das, A.; Chakraborty, B.; Piscanec, S.; Pisana, S.; Sood, A. K.; Ferrari, A. C. Phonon Renormalization in Doped Bilayer Graphene. *Phys. Rev. B: Condens. Matter Mater. Phys.* **2009**, *79*, 155417.

(28) Li, Z.; Liu, Y.; Lindsay, L.; Xu, Y.; Duan, W.; Pop, E. Size Dependence and Ballistic Limits of Thermal Transport in Anisotropic Layered Two-Dimensional Materials. *arXiv* **2017**; https://arxiv.org/abs/1711.02772 (accessed November 5, 2021).

(29) Yang, J.; Ziade, E.; Maragliano, C.; Crowder, R.; Wang, X.; Stefancich, M.; Chiesa, M.; Swan, A. K.; Schmidt, A. J. Thermal Conductance Imaging of Graphene Contacts. *J. Appl. Phys.* **2014**, *116*, No. 023515.

(30) Ding, Z.; Pei, Q. X.; Jiang, J. W.; Huang, W.; Zhang, Y. W. Interfacial Thermal Conductance in Graphene/MoS_2 Heterostructures. *Carbon* **2016**, *96*, 888−896.

(31) Zhang, J.; Hong, Y.; Yue, Y. Thermal Transport across Graphene and Single Layer Hexagonal Boron Nitride. *J. Appl. Phys.* **2015**, *117* (13), 134307.

(32) Li, B.; Wang, L.; Casati, G. Thermal Diode: Rectification of Heat Flux. *Phys. Rev. Lett.* **2004**, *93* (18), 184301.

(33) Chiritescu, C.; Cahill, D. G.; Nguyen, N.; Johnson, D.; Bodapati, A.; Keblinski, P.; Zschack, P. Ultralow Thermal Conductivity in Disordered, Layered WSe_2 Crystals. *Science* **2007**, *315* (5810), 351−353.

(34) Kadoya, K.; Matsunaga, N.; Nagashima, A. Viscosity and Thermal Conductivity of Dry Air in the Gaseous Phase. *J. Phys. Chem. Ref. Data* **1985**, *14* (4), 947−970.

(35) Leibfried, G.; Ludwig, W. Theory of Anharmonic Effects in Crystals. In *Solid State Physics*; Seitz, F., Turnbull, D., Eds.; Academic Press: New York, 1961; pp 276−444.

(36) Errea, I.; Calandra, M.; Mauri, F. Anharmonic Free Energies and Phonon Dispersions from the Stochastic Self-Consistent Harmonic Approximation: Application to Platinum and Palladium Hydrides. *Phys. Rev. B: Condens. Matter Mater. Phys.* **2014**, *89*, No. 064302.

(37) Nath, P.; Plata, J. J.; Usanmaz, D.; Al Rahal Al Orabi, R.; Fornari, M.; Nardelli, M. B.; Toher, C.; Curtarolo, S. High-Throughput Prediction of Finite-Temperature Properties Using the

https://doi.org/10.1021/acsnano.1c06299
ACS Nano 2021, 15, 19503−19512

Quasi-Harmonic Approximation. *Comput. Mater. Sci.* **2016**, *125*, 82−91.
(38) Ding, Z.; Jiang, J.-W.; Pei, Q.-X.; Zhang, Y.-W. In-Plane and Cross-Plane Thermal Conductivities of Molybdenum Disulfide. *Nanotechnology* **2015**, *26* (6), 065703.
(39) Chen, S.; Sood, A.; Pop, E.; Goodson, K. E.; Donadio, D. Strongly Tunable Anisotropic Thermal Transport in MoS_2 by Strain and Lithium Intercalation: First-Principles Calculations. *2D Mater.* **2019**, *6* (2), No. 025033.
(40) Gurarslan, A.; Yu, Y.; Su, L.; Yu, Y.; Suarez, F.; Yao, S.; Zhu, Y.; Ozturk, M.; Zhang, Y.; Cao, L. Surface-Energy-Assisted Perfect Transfer of Centimeter-Scale Monolayer and Few-Layer MoS_2 Films onto Arbitrary Substrates. *ACS Nano* **2014**, *8* (11), 11522−11528.
(41) Huxtable, S.; Cahill, D. G.; Fauconnier, V.; White, J. O.; Zhao, J. C. Thermal Conductivity Imaging at Micrometre-Scale Resolution for Combinatorial Studies of Materials. *Nat. Mater.* **2004**, *3*, 298−301.
(42) Olson, D. H.; Avincola, V. A.; Parker, C. G.; Braun, J. L.; Gaskins, J. T.; Tomko, J. A.; Opila, E. J.; Hopkins, P. E. Anisotropic Thermal Conductivity Tensor of β-$Y_2Si_2O_7$ for Orientational Control of Heat Flow on Micrometer Scales. *Acta Mater.* **2020**, *189*, 299−305.
(43) Kolmogorov, A. N.; Crespi, V. H. Registry-Dependent Interlayer Potential for Graphitic Systems. *Phys. Rev. B: Condens. Matter Mater. Phys.* **2005**, *71*, 235415.
(44) Lindsay, L.; Broido, D. Optimized Tersoff and Brenner Empirical Potential Parameters for Lattice Dynamics and Phonon Thermal Transport in Carbon Nanotubes and Graphene. *Phys. Rev. B: Condens. Matter Mater. Phys.* **2010**, *81*, 205441.
(45) Jiang, J.-W.; Park, H. S. Mechanical Properties of MoS_2/Graphene Heterostructures. *Appl. Phys. Lett.* **2014**, *105*, No. 033108.
(46) Liang, T.; Phillpot, S. R.; Sinnott, S. B. Parametrization of a Reactive Many-Body Potential for Mo − S Systems. *Phys. Rev. B: Condens. Matter Mater. Phys.* **2009**, *79*, 245110.
(47) Mishin, Y.; Farkas, D.; Mehl, M. J.; Papaconstantopoulos, D. A. Interatomic Potentials for Monoatomic Metals from Experimental Data and *ab Initio* Calculations. *Phys. Rev. B: Condens. Matter Mater. Phys.* **1999**, *59* (5), 3393−3407.
(48) Reshetniak, V. V.; Aborkin, A. V. Aluminum−Carbon Interaction at the Aluminum−Graphene and Aluminum−Graphite Interfaces. *J. Exp. Theor. Phys.* **2020**, *130* (2), 214−227.
(49) Ebnonnasir, A.; Narayanan, B.; Kodambaka, S.; Ciobanu, C. Tunable MoS_2 Bandgap in MoS_2-Graphene Heterostructures. *Appl. Phys. Lett.* **2014**, *105*, No. 031603.
(50) Baskin, Y.; Meyer, L. Lattice Constants of Graphite at Low Temperatures. *Phys. Rev.* **1955**, *100* (2), 544.
(51) Plimpton, S. Fast Parallel Algorithms for Short-Range Molecular Dynamics. *J. Comput. Phys.* **1995**, *117*, 1−19.
(52) Li, Z.; Xiong, S.; Sievers, C.; Hu, Y.; Fan, Z.; Wei, N.; Bao, H.; Chen, S.; Donadio, D.; Ala-Nissila, T. Influence of Thermostatting on Nonequilibrium Molecular Dynamics Simulations of Heat Conduction in Solids. *J. Chem. Phys.* **2019**, *151*, 234105.

https://doi.org/10.1021/acsnano.1c06299
ACS Nano 2021, 15, 19503−19512

Supplementary Materials for:

Engineering Thermal Transport across Layered Graphene-MoS_2 Superlattices

Aditya Sood[1,†], Charles Sievers[2,#], Yong Cheol Shin[1,#], Victoria Chen[1], Shunda Chen[2], Kirby K. H. Smithe[1], Sukti Chatterjee[3], Davide Donadio[2,*], Kenneth E. Goodson[4,5], Eric Pop[1,5,*]

[1]Department of Electrical Engineering, Stanford University, Stanford CA 94305, USA

[2]Department of Chemistry, University of California, Davis CA 95616, USA

[3]Applied Materials Inc., Santa Clara CA 95054, USA

[4]Department of Mechanical Engineering, Stanford University, Stanford CA 94305, USA

[5]Department of Materials Science and Engineering, Stanford University, Stanford CA 94305, USA

[†]Present address: Stanford Institute for Materials and Energy Sciences, SLAC National Accelerator Laboratory, Menlo Park CA 94025, USA

[#]Contributed equally

*ddonadio@ucdavis.edu, epop@stanford.edu

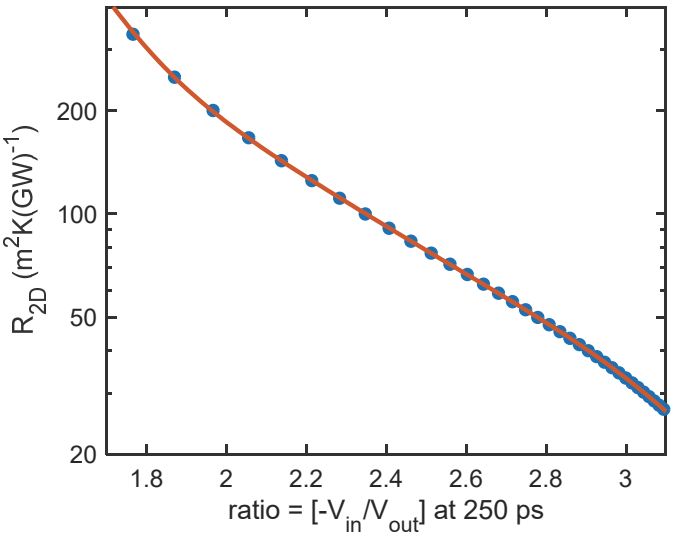

Figure S1: Transfer function relating the TDTR ratio signal (= $-V_{in}/V_{out}$) at +250 ps to the cross-plane thermal resistance of the 2D stack at the Al/SiO_2 interface, R_{2D}. Blue points are obtained from a solution to the 3D multilayer thermal model, while the red curve is a fit to a 6th order polynomial. The multilayer stack, from top to bottom, is: Al (80 nm)/{2D stack}/SiO_2 (90 nm)/Si.

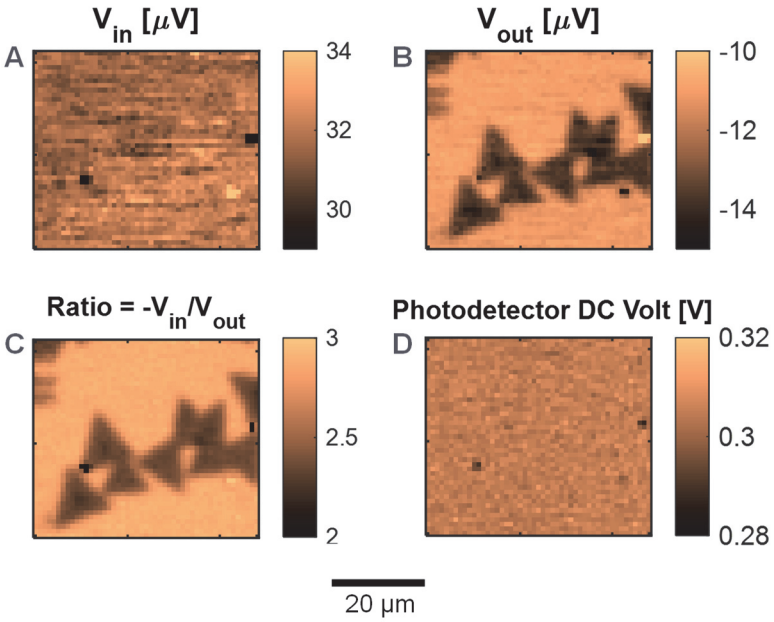

Figure S2: Maps of raw TDTR signals showing the (A) in-phase voltage V_{in}, (B) out-of-phase voltage V_{out}, (C) ratio = $-V_{in}/V_{out}$, and (D) DC probe reflectivity measured by the photodetector. Signals (A)-(C) are at a probe delay time of +250 ps. Because the sample is coated by an optically-opaque Al transducer layer, the DC probe reflectivity is uniform. Variations in the thermal resistance of the 2D interface between Al and SiO_2 appear largely as variations in the out-of-phase voltage (and thus the ratio). The ratio signal is converted to thermal resistance of the 2D interface using the transfer curve shown in **Fig. S1**.

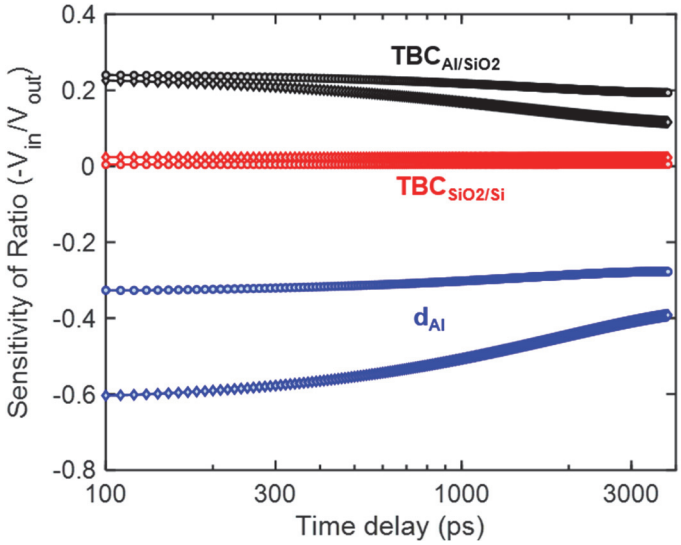

Figure S3: Sensitivity of the TDTR ratio signal to various parameters. TBC is the thermal boundary conductance = (thermal boundary resistance)$^{-1}$. The sensitivity coefficient for a parameter α is calculated as: $S_\alpha = \partial\log(Ratio)/\partial\log(\alpha)$, where $Ratio = -V_{in}/V_{out}$. Here, we examine the sensitivity to three parameters: (1) TBC at the Al/SiO_2 interface, which is equal to $(R_{2D})^{-1}$, and is the quantity we are interested in measuring (black markers), (2) TBC at the SiO_2/Si interface (red markers), and (3) Al transducer thickness (blue markers). Two sets of curves are plotted for extreme values of R_{2D}: diamonds for R_{2D} = 50 $m^2K(GW)^{-1}$, circles for R_{2D} = 200 $m^2K(GW)^{-1}$.

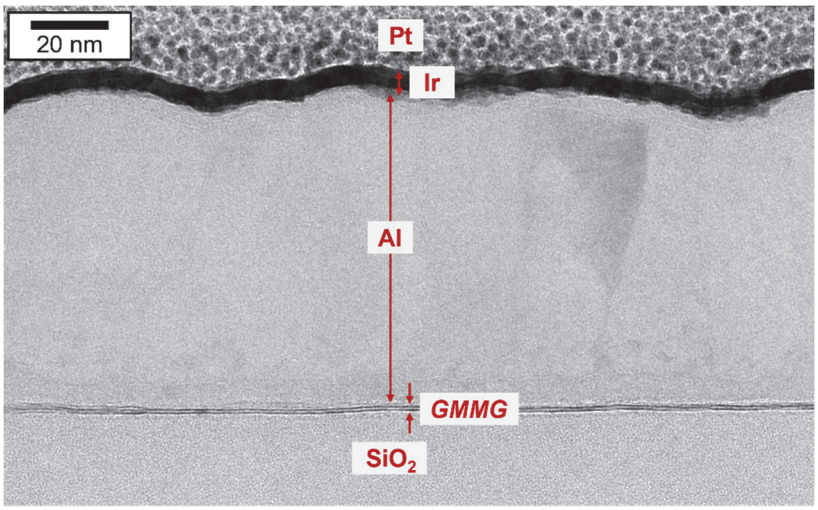

Figure S4: Cross sectional transmission electron micrograph (TEM) of a GMMG region in sample D2. The thickness of the Al transducer is 80 ± 2 nm (error bars based on the root-mean-square variation in thickness). The Ir and Pt layers are deposited during TEM sample preparation.

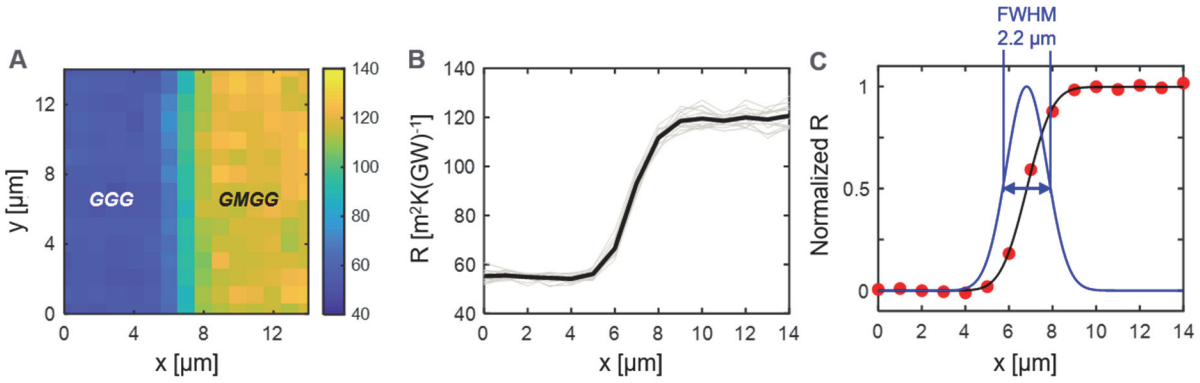

Figure S5: Spatial resolution of TDTR thermal resistance microscopy. (A) Thermal resistance map across a sharp junction between regions of the sample with GGG and GMGG stacking, *i.e.* the region on the right side has an additional MoS_2 monolayer inserted between the first two graphene layers. (B) Horizontal line cuts taken at 15 locations on the map (light grey) and the average of these line cuts (solid black). (C) Error function fit (black curve) of the average line cut data (red markers). Derivative of the error function curve gives a Gaussian (blue curve) with full-width half-maximum (FWHM) spatial resolution of 2.2 μm.

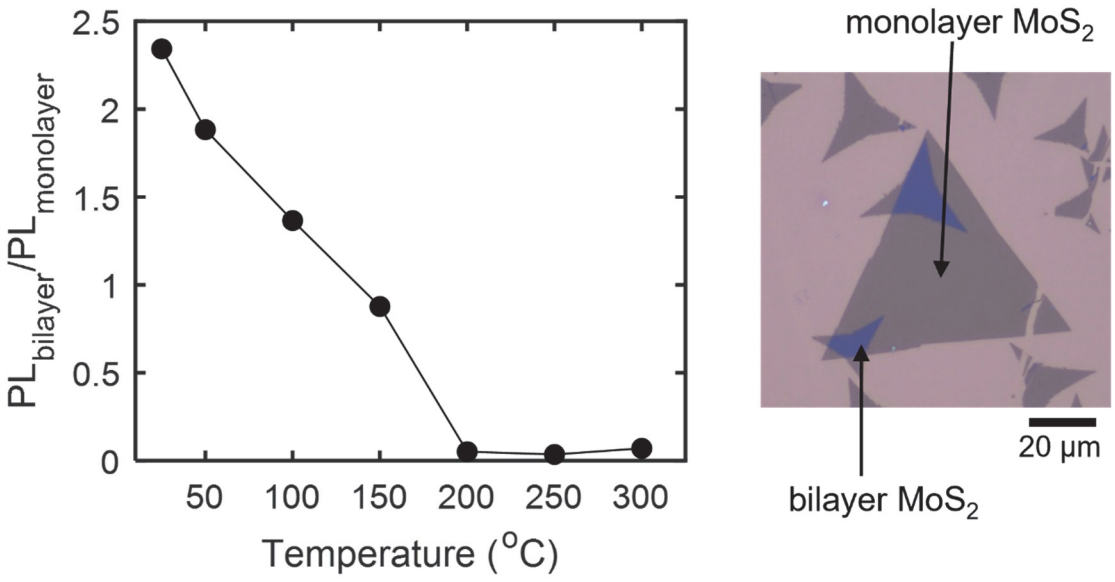

Figure S6: Temperature-dependent *in-situ* photoluminescence (PL) measurements. Plot on the left shows the intensity contrast between layer-by-layer transferred bilayer and monolayer MoS_2 regions. Significant quenching is observed above 200°C, consistent with stronger electronic coupling between the MoS_2 monolayers. Optical image on the right shows the locations of the two regions.

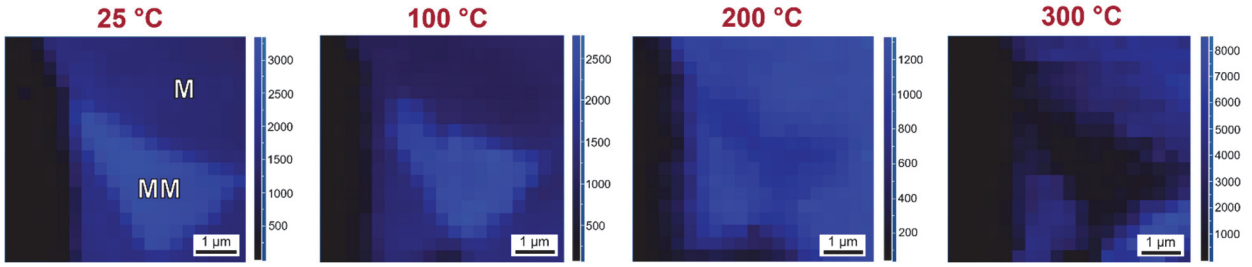

Figure S7: PL maps taken at different temperatures showing enhanced intensity quench in layer-by-layer transferred bilayer MoS_2 (labelled MM) relative to monolayer MoS_2 (labelled M) with increasing temperature.

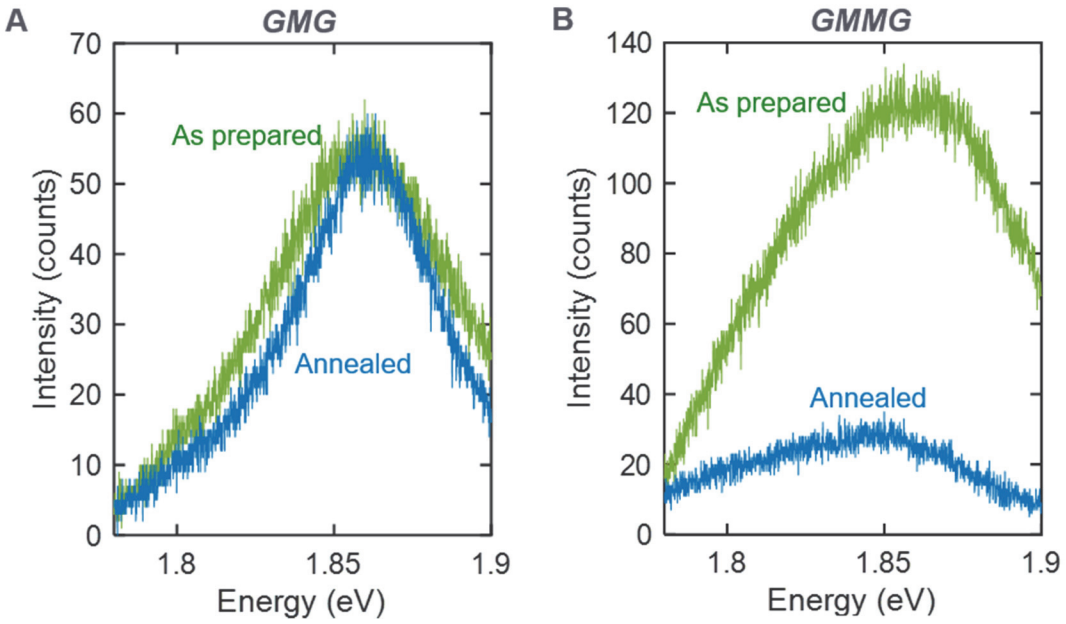

Figure S8: MoS_2 PL point spectra of (A) GMG and (B) GMMG regions of sample D2, showing the effect of annealing at 350°C for 3 hours under high vacuum (7 µTorr). No PL quenching is observed in GMG suggesting that annealing does not significantly modify the electronic coupling between graphene and MoS_2. In GMMG, the PL intensity is initially twice that in GMG, and is quenched upon annealing, due to the enhanced electronic coupling between the two MoS_2 monolayers.

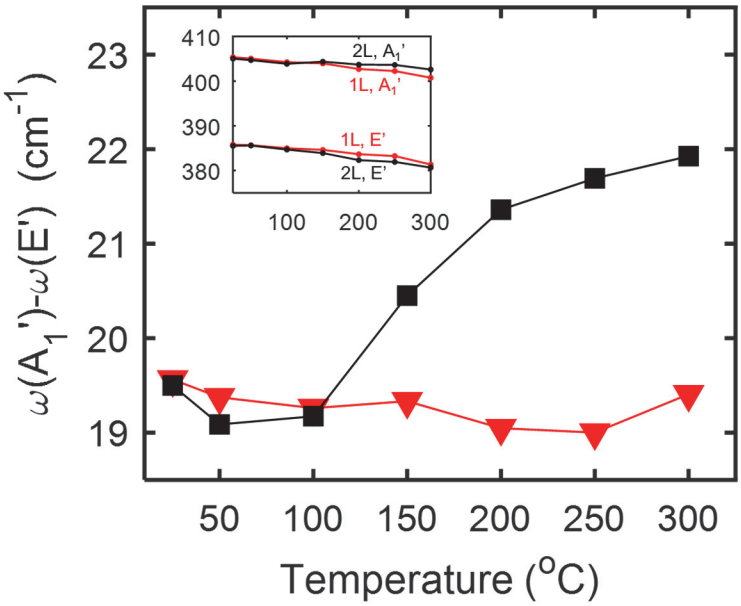

Figure S9: Temperature-dependent *in-situ* Raman measurements. Main plot shows the frequency difference between the A_1' and E' modes as a function of temperature, for layer-by-layer transferred bilayer (black squares) and monolayer (red triangles) MoS_2. Inset shows the frequencies (in cm^{-1}) of the A_1' and E' modes for bilayer ('2L' black) and monolayer ('1L' red).

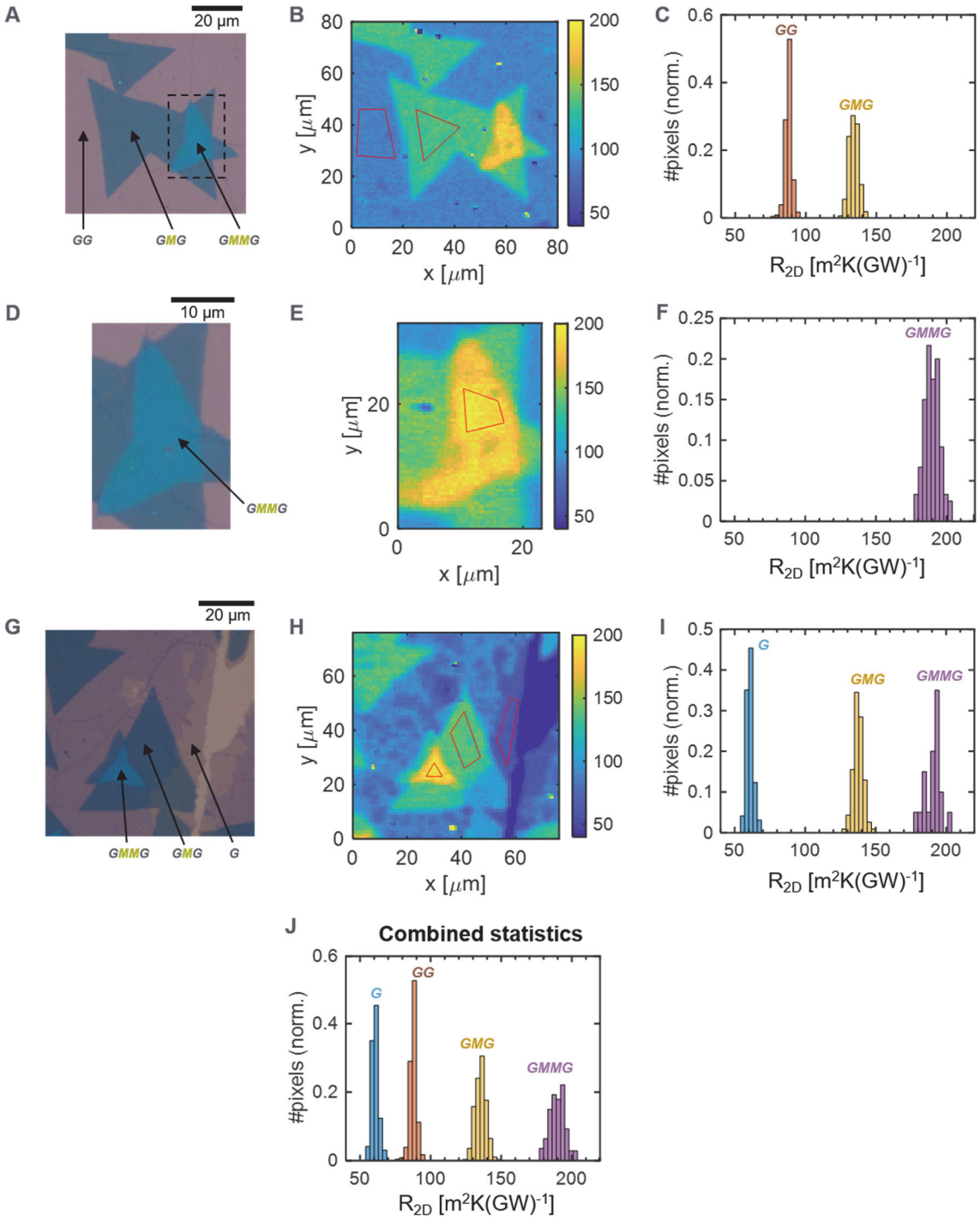

Figure S10: Comprehensive data on sample D1, showing optical micrographs, TDTR thermal resistance maps, and statistics. Regions of interest (ROIs) based on which the histograms are plotted are marked by the red polygons on the TDTR maps. (A)-(C) Region 1, providing data on GG and GMG regions. (D)-(F) Region 2, which zooms into the area enclosed within the dashed lines in (A), providing high-resolution data on GMMG. This TDTR map is measured with a step size of 500 nm. (G)-(I) Region 3, providing data on G, GMG, and GMMG. (J) Combined statistics taken from all 3 regions. In (C), (F), (I), and (J), each distribution is normalized by the number of pixels in the ROI.

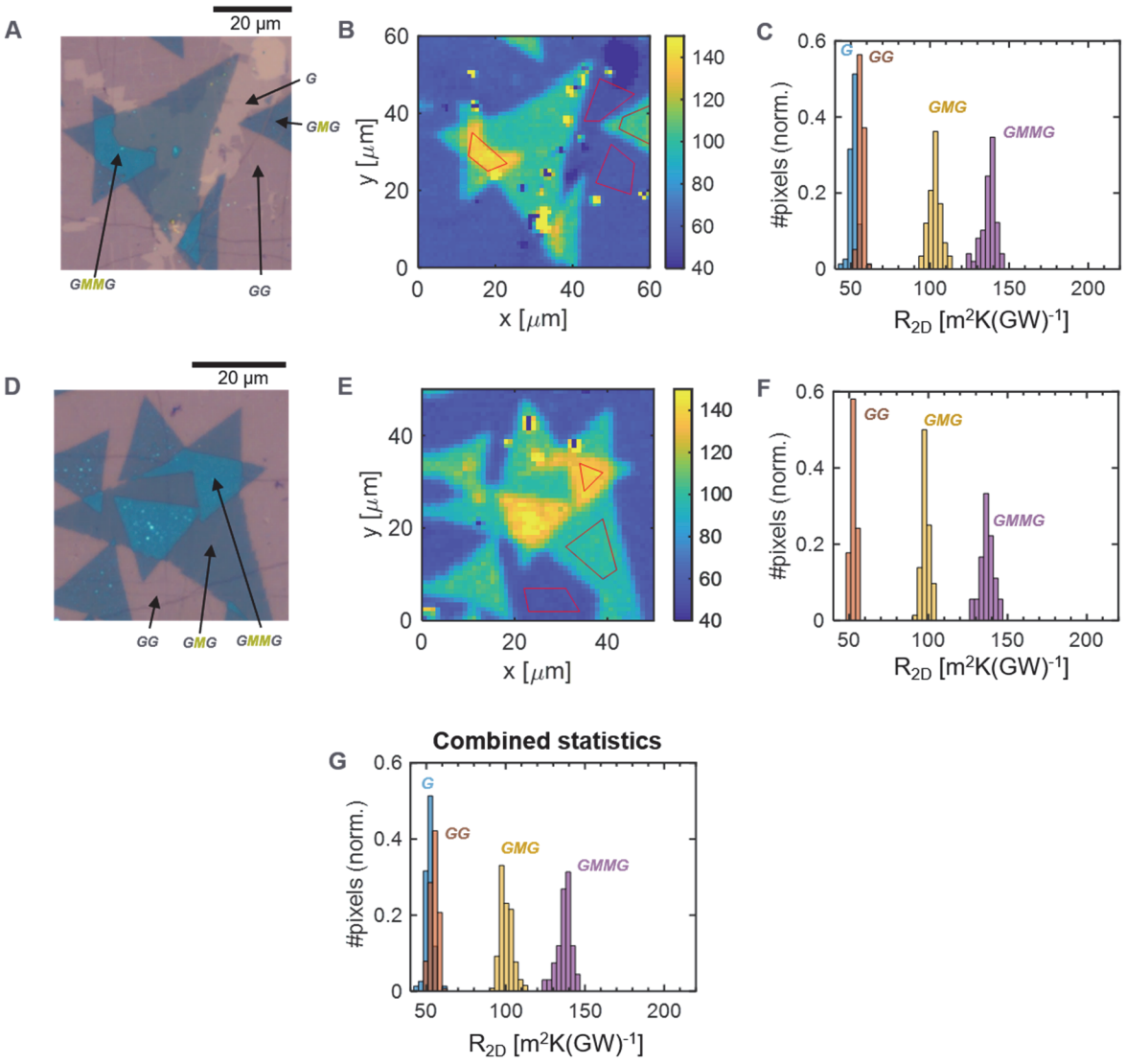

Figure S11: Comprehensive data on sample D2, showing optical micrographs, TDTR thermal resistance maps, and statistics. Regions of interest (ROIs) based on which the histograms are plotted are marked by the red polygons on the TDTR maps. (A)-(C) Region 1, providing data on G, GG, GMG and GMMG regions. (D)-(F) Region 2, providing data on GG, GMG and GMMG regions. (G) Combined statistics taken from both regions. In (C), (F), and (G), each distribution is normalized by the number of pixels in the ROI.

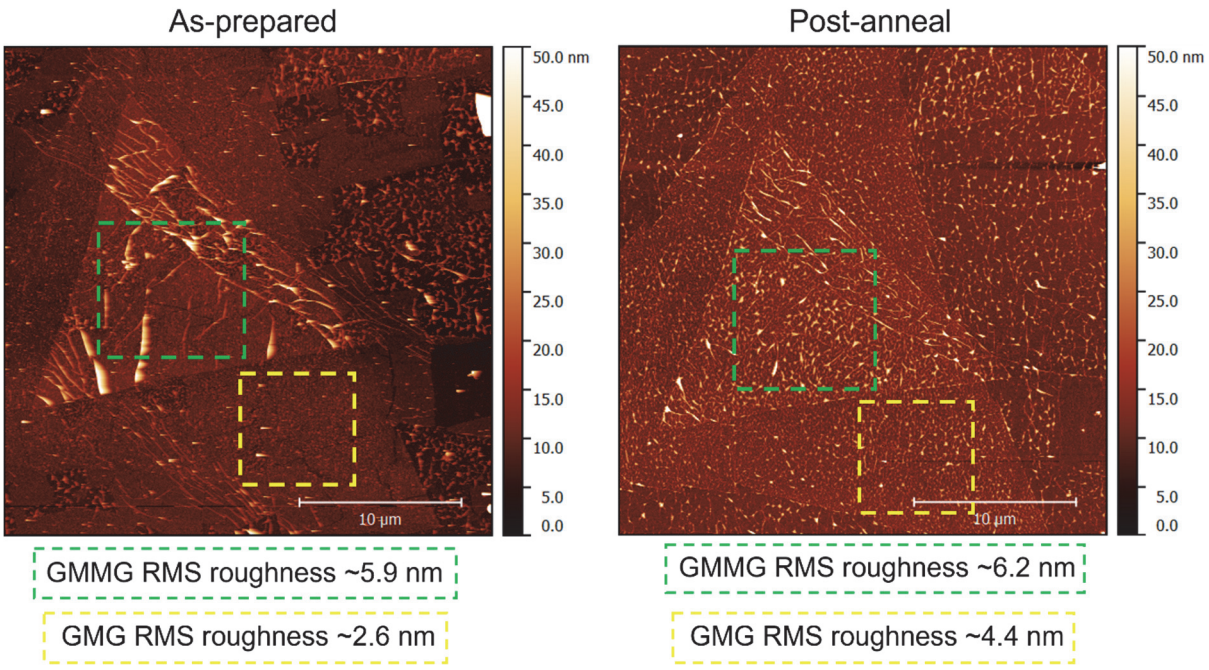

Figure S12: Effect of annealing on sample roughness. Atomic force microscopy (AFM) scans of the same region of the sample before (left) and after (right) annealing. The green and yellow dashed boxes are regions with GMMG and GMG stacking, respectively. The root-mean-square (rms) roughness of the GMMG region increases from ~5.9 to ~6.2 nm, and that of the GMG region increases from ~2.6 to ~4.4 nm.

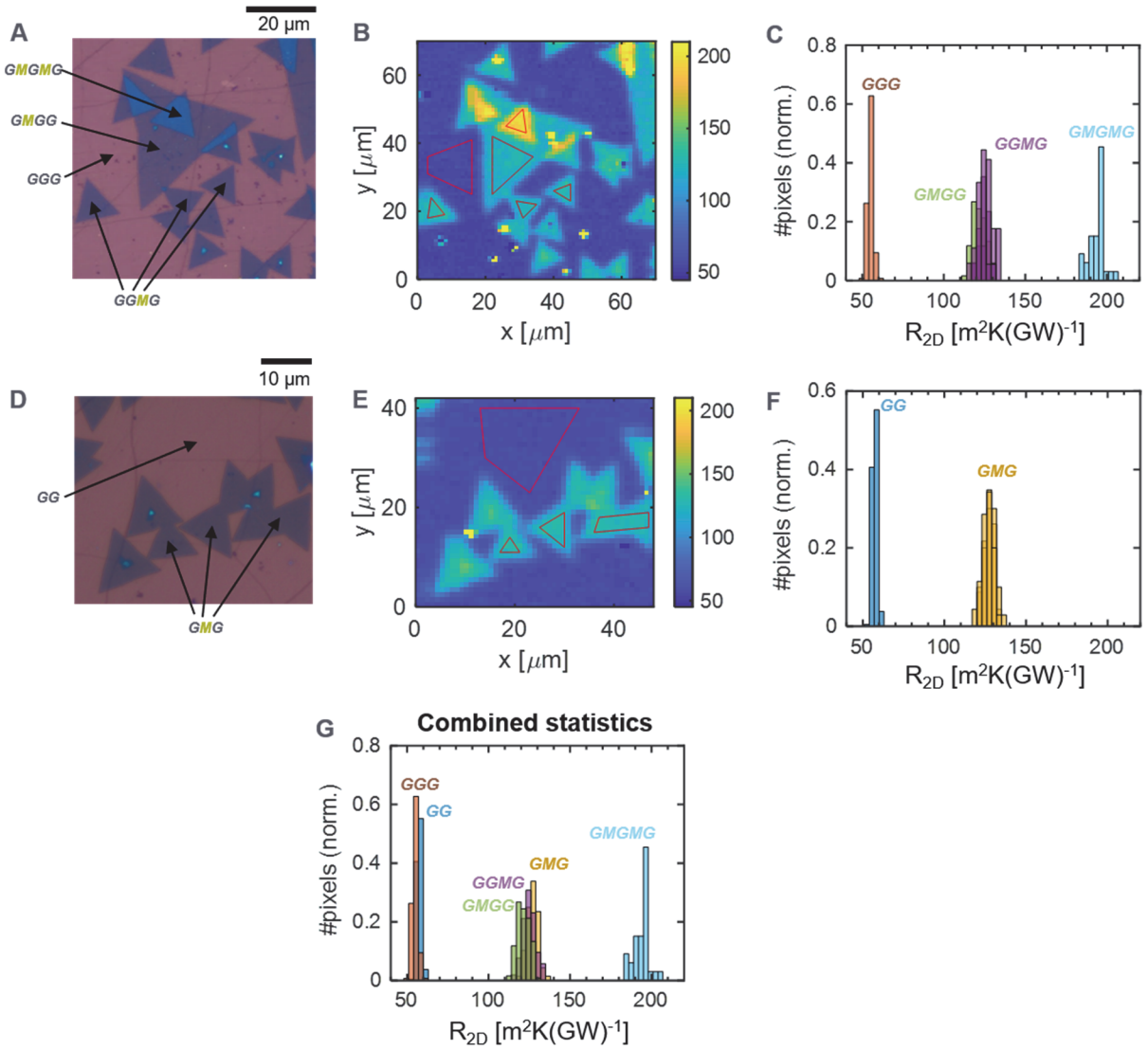

Figure S13: Comprehensive data on sample D3, showing optical micrographs, TDTR thermal resistance maps, and statistics. Regions of interest (ROIs) based on which the histograms are plotted are marked by the red polygons on the TDTR maps. (A)-(C) Region 1, providing data on GGG, GGMG, GMGG, and GMGMG regions. (D)-(F) Region 2, providing data on GG and GMG regions. (G) Combined statistics taken from both regions. In (C), (F), and (G), each distribution is normalized by the number of pixels in the ROI.

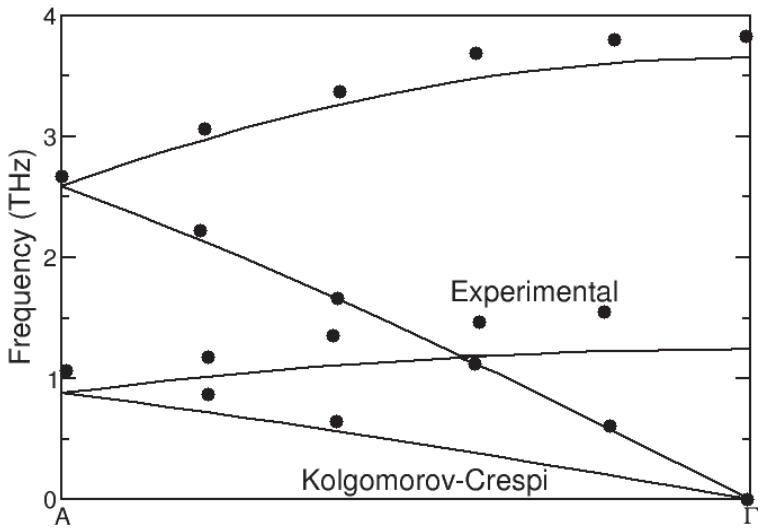

Figure S14: Phonon dispersion of graphite along the Γ-A direction computed with a modified Kolmogorov-Crespi (KC) potential (lines). The reparametrization of the KC potential involved lowering the exponential prefactor C_0 by 2 eV. This prefactor is directly related to the change in potential energy resulting from layer-layer relative in-plane translations. This was done to tune the softness of the transverse acoustic modes to produce better agreement with experimental phonon dispersion (filled circles) from Ref. 1.

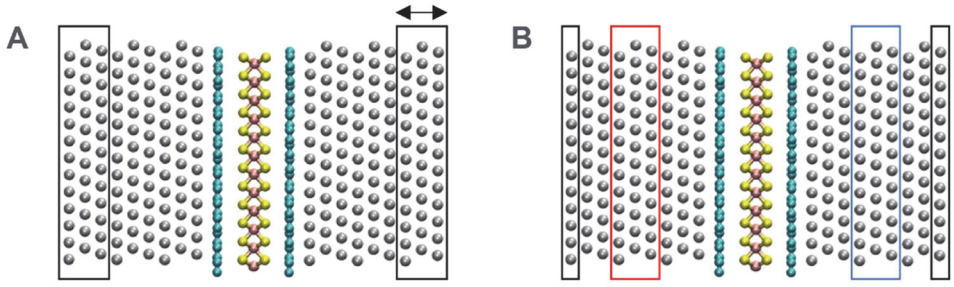

Figure S15: Simulation configurations. Grey atoms are aluminum, cyan atoms are carbon, pink atoms are molybdenum, yellow atoms are sulfur. Black boxes enclose atoms that are kept fixed in the calculations. (A) During QHA FEM, the outer three layers of aluminum atoms are fixed. The set of fixed atoms to the right of the device is displaced relative to the rest of the device to relax the cell (indicated by a double-headed arrow). (B) During NEMD, the outermost layer of aluminum atoms on either side is fixed. The atoms in the red box represent the heat source which was set to 350 K, and the atoms in the blue box represent the heat sink which were thermostatted to 250 K using a Langevin thermostat. The rest of the device was run in the NVE ensemble.

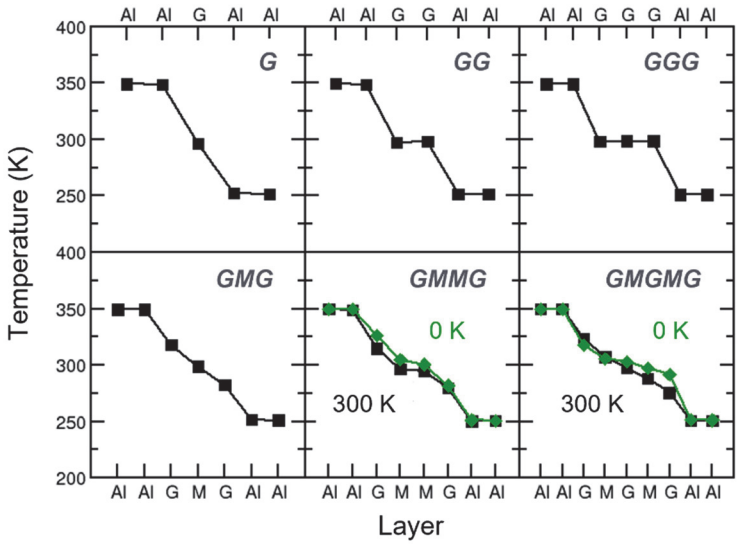

Figure S16: Temperature profiles averaged over the last 500 ps of each NEMD simulation (with 10 fs intervals). Each device shows large jumps in the temperature profile at the Al-G interfaces indicating a larger resistance at these interfaces. The GG and GGG systems exhibit relatively low resistances at the G-G homojunctions compared to the Al-G heterojunctions. The GMMG shows that the M-M homojunction exhibits lower resistance than either the Al-G or G-M heterojunctions. The GMMG and GMGMG devices also have their 0 K optimized structures run at the same NEMD conditions for reference, to see the effects of thermal expansion. We see that for GMGMG, as the device expands, the resistances of the G-M interfaces grow relative to the Al-G interfaces, however, for GMMG this is not as clearly the case. As the devices expand, the G and M layers become thermally decoupled from one another, which contributes to an increase in the overall thermal resistance.

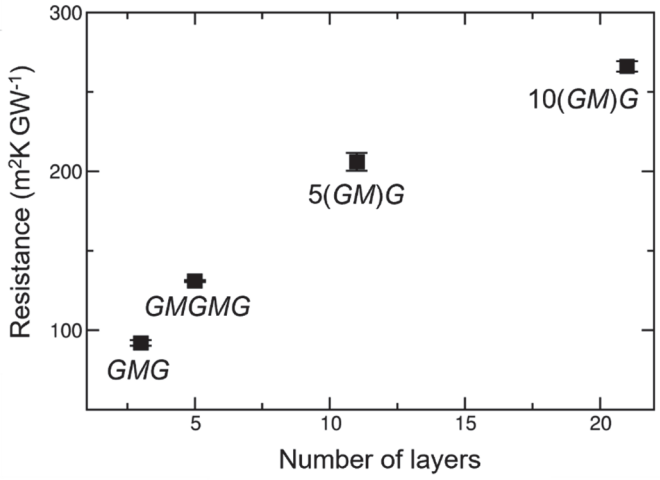

Figure S17: Thermal resistance of n ×(GM)G ideal stacks with n = 1, 2, 5, 10 from NEMD simulations. Sub-linear increase of thermal resistance indicates that phonon transport is not yet diffusive for heterostructures with < 21 layers, and their overall thermal resistivity decreases as the stacks get thicker.

Table S1: Error propagation analysis

Stack	Δ_1: Al thick ±2 nm. (%)	Δ_2: spot size ±2.5%. (%)	Δ_3: k_{SiO2}±0.1 $Wm^{-1}K^{-1}$. (%)	Δ_4: ref phase ±8 mrad. (%)	Δ_5: std. dev. (%)	Δ_6: inter-sample. (%)	**Total error, Δ (%)**
G	7.0	10.1	9.9	11.9	4.4	-	**20.2**
GG	7.0	10.1	9.9	11.9	4.5	2	**20.4**
GGG	7.0	10.1	9.9	11.9	3.2	-	**20.0**
GMG	4.3	8.4	3.5	8.9	4.1	7	**15.7**
GGMG	4.3	8.4	3.5	8.9	2.9	-	**13.8**
GMGG	4.3	8.4	3.5	8.9	3.2	-	**13.8**
GMMG	3.7	8.2	2.6	7.5	3.2	-	**12.4**
GMGMG	2.7	9.0	2.0	8.0	2.5	-	**12.7**

Six sources of error are considered (labeled Δ_1 to Δ_6). The first four are due to uncertainties in the: (1) thickness of the Al transducer, ±2 nm. (2) rms laser spot size, ±2.5%, (3) thermal conductivity of SiO_2, ±0.1 $Wm^{-1}K^{-1}$, (4) lock-in reference phase, ±8 mrad – estimated by dividing the rms noise in V_{out} (between -100 ps and +50 ps) by the jump in V_{in} at time-zero. The last two are due to: (5) spatial variations within a sample, determined from the standard deviation of the thermal resistance histograms. (6) Sample-to-sample variation, only relevant for GG and GMG where the same stack is found in more than one sample (D2 and D3). The total error is obtained by adding up the individual contributions in quadrature, $\Delta = (\Delta_1^2 + \Delta_2^2 + \Delta_3^2 + \Delta_4^2 + \Delta_5^2 + \Delta_6^2)^{1/2}$.

Supplementary References

(1) Nicklow, R.; Wakabayashi, N.; Smith, H. G. Lattice Dynamics of Pyrolytic Graphite. *Phys. Rev. B* **1972**, *5* (12), 4951–4962. https://doi.org/10.1103/PhysRevB.5.4951.